Influence of nitrogen oxides and volatile organic compounds emission changes on

tropospheric ozone variability, trends and radiative effect

Suvarna Fadnavis[1], Yasin Elshorbany[2], Jerald Ziemke[3], Brice Barret[4], Alexandru Rap[5], PR Satheesh Chandran [1], Richard J. Pope[5], Vijay Sagar[1], Domenico Taraborrelli[6], Eric Le Flochmoen[34], Juan Cuesta[7], Catherine Wespes[8], Folkert Boersma[9,10], Isolde Glissenaar[9], Isabelle De Smedt[11], Michel Van Roozendael[11], Hervé Petetin[12], Isidora Anglou[9]

[1]Center for Climate Change Research, Indian Institute of Tropical Meteorology, MoES, Pune, India
[2]School of Geosciences, College of Arts and Sciences, University of South Florida, St. Petersburg, FL, USA
[3]NASA Goddard Space Flight Center, Greenbelt, Maryland, USA
[4]LAERO/OMP, Université Paul Sabatier, Université de Toulouse-CNRS, Toulouse, France
[5]School of Earth and Environment, University of Leeds, Leeds, UK; National Centre for Earth Observation, University of Leeds, Leeds, UK
[6]Institute of Climate and Energy Systems, ICE-3: Troposphere, Forschungszentrum Jülich GmbH, Jülich, Germany,
[7]University Paris Est Creteil and Université Paris Cité, CNRS, LISA, F-94010 Créteil, France
[8]Université libre de Bruxelles (ULB), Spectroscopy, Quantum Chemistry and Atmospheric Remote Sensing, Brussels, Belgium
[9]Royal Netherlands Meteorological Institute (KNMI), De Bilt, The Netherlands
[10]Wageningen University, Environmental Sciences Group, Wageningen, The Netherlands
[11]Belgian Institute for Space Aeronomy, Brussels, Belgium
[12]Barcelona Supercomputing Center, Barcelona, Spain

Corresponding author email: suvarna@tropmet.res.in

34 **Abstract**

35 Ozone in the troposphere is a prominent pollutant whose production is sensitive to the

36 emissions of nitrogen oxides (NOx) and volatile organic compounds (VOC). Here, we assess

37 the variation of tropospheric ozone levels, trends, ozone photochemical regimes, and radiative

38 effects using the ECHAM6–HAMMOZ chemistry-climate model for the period 1998–2019

39 and satellite measurements. The global mean simulated trend in Tropospheric Column Ozone

40 (TRCO) for the study period (1998–2019) is 0.89 ppb decade−1. During the overlapping period

41 with OMI/MLS observations (2005–2019), the simulated global mean TRCO trends (1.58 ppb

42 decade−1) show fair agreement with OMI/MLS estimates (1.4 ppb decade−1). The simulations

43 for doubling emissions of NOx (DoubNOx), VOCs (DoubVOC), halving of emissions NOx

44 (HalfNOx) and VOCs (HalfVOC) show nonlinear responses to ozone trends and tropospheric

45 ozone photochemical regimes. The DoubNOx simulations show VOC–limited regimes over

46 Indo-Gangetic-Plains, Eastern-China, Western-Europe, and the Eastern-US, while HalfNOx

47 simulations show NOx–limited regimes over North-America and Asia. Emissions changes in

48 NOx (DoubNOx/HalfNOx) influence the shift in tropospheric ozone photochemical regimes

49 compared to VOCs (DoubVOC/HalfVOC).

51 Further, we provide estimates of tropospheric ozone radiative effects (TO3RE). The estimated

52 global mean TO3RE during 1998–2019 from the CTL simulations is 1.21 Wm−2. The global

53 mean TO3RE shows enhancement by 0.36 W m−2 in DoubNOx simulations than CTL. While

54 TO3RE shows a reduction in other simulations compared to CTL (DoubVOC: -0.005 Wm−2;

55 HalfNOx: -0.12 Wm−2; and HalfVOC: -0.03 Wm−2). We show that emissions changes in

56 anthropogenic NOx cause higher changes in TO3RE than anthropogenic VOCs.

57   Key words: Tropospheric ozone, trends, ozone photochemical regimes; ozone radiative effect.

58   FNR; ECHAM6-HAMMOZ model simulations.

59

1. Introduction

Tropospheric ozone, a major air pollutant, has been a pressing issue in recent decades due to its detrimental effect on human health and ecosystem productivity and as a short-term climate forcer (Riese et al. 2012; Gulev et al., 2021; Wang et al., 2022). Considering these harmful impacts, the assessment of tropospheric ozone levels and trends are being conducted frequently (Gaudel et al., 2018; Mills et al., 2018; Tarasick et al., 2019). Ozone trends are being assessed from surface observations, in-situ and ground-based measurements, satellite retrievals, and model simulations (Cooper et al., 2014; Cohen et al., 2018; Young et al., 2018; Tarasick et al., 2019; Archibald et al., 2020). The latest IPCC AR6 reported an enhancement in free tropospheric ozone by $2-7\%$ decade^{-1} in the northern mid-latitudes, $2-12\%$ per decade in the tropics, and $<5\%$ decade^{-1} in southern mid-latitudes (Gulev et al., 2021; Szopa et al., 2021). The Tropospheric Ozone Assessment Reports (TOAR) have documented global increases of tropospheric column ozone (TRCO) in the 20th century (Cooper et al., 2014; Lefohn et al., 2017; Schultz et al., 2017; Fleming et al., 2018; Gaudel et al., 2018; Mills et al., 2018; Young et al., 2018; Tarasick et al., 2019). Increasing tropospheric trends are explained by enhanced anthropogenic emissions (Cooper et al., 2014; Zhang et al., 2016) and modulation by climate variability (Lin et al., 2014; Lu et al., 2018). Several studies have documented increasing trends in TRCO across various regions and different time periods.

For instance, enhancement in TRCO trends globally using measurements from multiple sources such as In-service Aircraft for a Global Observing System database (IAGOS) and ozonesondes and GEOS–Chem model simulation revealed increasing trend of 2.7 ± 1.7 and 1.9 ± 1.7 ppb decade^{-1} between 1995 and 2017 (Wang et al., 2022). Additionally, Fiore et al. (2022) also found increasing trends ranging from 0.6 to 2.5 ppb decade^{-1} from 1950 to 2014 globally based on the available limited surface ozone records~~IAGOS measurements~~ and the Community Earth System, version-2, the Whole Atmosphere Community Climate Model, version-6 (CESM2–WACCM6) model study. Furthermore, trends in TRCO are stronger in the Northern Hemisphere (NH) than Southern Hemisphere (SH) due to larger anthropogenic emissions (Monks et al., 2015). Ozone Monitoring Instrument (OMI) and Microwave Limb Sounder (MLS) observations from 2005 until 2010 show annual TRCO ~~trends~~burden averaged over the NH exceed the SH by 4% at low latitudes ($0° - 25°$), by 12% at mid-latitudes ($25° - 50°$), and by 18% at high latitudes ($50° - 60°$) (Cooper et al., 2014). CMIP6 models also showe~~d~~

that the tropospheric ozone burden increased by 44 % in 2005 – 2014 compared to 1850 (Griffiths et al., 2021). Recently, studies have reported a decrease in TRCO trends globally after the Corona–Virus Disease 2019 (COVID–19) outbreak e.g., Chang et al. (2022, 2023), and Steinbrecht et al. (2021). Also, Putero et al. (2023) show widespread ozone decreases at high-elevation sites due to the COVID–19 lockdown. However, our study period (1998–2019) excludes the COVID–19 associated emission changes.

~~The trends in surface ozone have grown during the last century; however, a few locations show decreasing trends (Cooper et al., 2014). The UKESM1 model simulations show that global mean surface ozone increased by ~28% throughout the twentieth century (Archibald et al., 2020). The set of lower tropospheric and surface ozone measurements in the NH shows an increase in ozone by 30%–70% since the middle of the 20th Century (Gulev et al., 2021). Recent observations from UV-absorption analyzers from 2000 – 2021 in southwestern Europe show an increase in ozone trends of 2.2 ± 0.3 ppb decade^{-1} (Adame et al., 2022). Cooper et al. (2014) reported that surface ozone trends have varied over different regions from 1990 until 2010. In Western Europe, ozone concentration increased in the 1990s, followed by a levelling off or decrease since 2000. Analysis of monthly surface ozone anomaly data from 2000 to 2018 shows the strongest negative trend of -2.8 ± 1.1 ppb decade^{-1} at the Gothic station (41° N, 2.1° E) and the strongest positive trend of 2.2 ± 0.9 ppb decade^{-1} at American Samoa (14° S, 171° W) (Cooper et al., 2014). Lu et al. (2018) reported that the surface ozone trends varied between 0.17 % to 0.81 % in the SH from 1990 to 2015.~~ ~~CMIP6 models showed that the tropospheric ozone burden increased by 44 % in 2005 – 2014 compared to 1850 (Griffiths et al., 2021).~~

Nitrogen oxides (NOₒx; NO+NO$_2$) and~~or~~ volcanic organic compounds (VOC) are the major precursors that define ozone photochemical regimes (Duncan et al 2010). Information on ozone photochemical regimes is of utmost importance to know ozone (O$_3$) levels. However, the non-linearity in the O$_3$ – NOx – VOC chemistry has always posed a challenge in identifying photochemical regimes. The regime is called NOx–limited if the ozone production is directly related to a change in NOx~~, with no impact~~rather than from VOC perturbations. Whereas the region where ozone production is regulated by the ambient availability of VOCs is called VOC–limited (Sillman et al., 1990; Kleinman, 1994). The ratios such as ozone to oxidized nitrogen species (O$_3$/(NOy-NOx), where NOy is the total reactive nitrogen), formaldehyde to

124 total reactive nitrogen (HCHO/NO~~o~~y), formaldehyde to nitrogen dioxide (HCHO/NO$_2$),

125 hydrogen peroxide to nitric acid (H_2O_2/HNO_3) are adopted to diagnose the ozone

126 photochemical regimes (e.g., Sillman, 1995; Martin et al., 2004; Duncan et al., 2010). Among

127 these, the most widely used indicator to identify regimes is the Formaldehyde (HCHO) to

128 Nitrogen dioxide (NO$_2$) Ratio (FNR) (Martin et al., 2004; Duncan et al., 2010). In our study,

129 we adopt FNR to identify NOx–limited or VOC–limited regimes. On par with the current effort

130 to mitigate ozone pollution, it is important to understand how the changes in emissions of NOx

131 and VOC affect the ozone photochemical regimes and trends (Jin et al., 2017, 2020).

132

133 Ozone is the third strongest anthropogenic greenhouse gas ~~forcer~~, also called a short-

134 term~~lived~~ climate forcer, producing a global average radiative forcing of 0.47 [0.24 to 0.71 W

135 m^{-2}] [5% to 95% uncertainty range] (Forster et al., 2021). Recent studies showed ozone

136 effective radiative forcing (ERF) of 0.51 [0.25 to 0.76] W m^{-2} during 1750 – 2023 (Forster et

137 al., 2024). ~~The global mean radiative forcing of +0.35 W.m^{-2} due to ozone during 1750 – 2011~~

138 ~~is reported by Myhre et al. (2013). The CMIP6 model from 1850 to 2014 estimates an ozone~~

139 ~~radiative forcing of 0.39 W.m^{-2} [0.27 to 0.51] (Skeie et al., 2020).~~ The knowledge of ozone

140 radiative forcing due to changes in anthropogenic emissions of NOx and VOC will help to

141 assess climate change. Therefore, we also show the impacts of enhanced or reduced emissions

142 of NOx and VOC on ozone radiative effect~~forcing~~ in addition to ozone trends and

143 photochemical regimes. To achieve this, we conducted sensitivity experiments by doubling and

144 halving global NOx and VOC emissions using the state–of–the–art chemistry-climate model

145 ECHAM6–HAMMOZ for the period 1998–2019. This approach of increase/decrease of

146 emissions is important to understand nonlinear response of ozone to emission changes. These

147 experiments are helpful for designing emission implementation strategies (e.g., Zhang et al.,

148 2021; Wang et al., 2023). The paper is outlined as follows: satellite data and the model

149 experimental setup are given in section 2, and results are given in section 3, which includes a

150 comparison of simulated tropospheric column ozone with satellite data and estimated ozone

151 trends. Discussions on ozone photochemical regimes and their trends are made in sections 4 to

152 6. Estimates of ozone radiative effects are given in section 7. Conclusions are made in section

153 8.

154

2.   Satellite data and model experiments

2.1.   OMI Satellite Data.

We include OMI/MLS tropospheric column ozone (TRCO) for October 2004 – December 2019 and OMI NO_2, HCHO data for latitude range 60° S – 60° N (Ziemke et al., 2006; De Smedt et al., 2021; Lamsal et al., 2021). OMI/MLS TRCO is determined by subtracting MLS stratospheric column ozone (SCO) from OMI total column ozone each day at each grid point. Tropopause pressure used to determine the SCO invoked the World Meteorological Organization (WMO) 2 K km^{-1} lapse-rate definition from the NCEP reanalysis. The MLS data used to obtain SCO were derived from the MLS v4.2 ozone profiles. We estimate 1σ precision for the OMI/MLS monthly mean gridded TRCO product to be about 1.3 DU. Adjustments for drift calibration and other issues (e.g., OMI row anomaly) affecting OMI/MLS TRCO are discussed by Ziemke et al. (2019) and Gaudel et al. (2024).

We used OMI monthly mean Level 3 (L3) data for NO_2 and HCHO (https://doi.org/10.18758/h2v1uo6x) that were produced in the context of the ESA CCI+ precursors for aerosols and ozone project (De Smedt et al., 2021; Anglou et al., 2024). The datasets consist of the monthly mean tropospheric column densities for NO_2 and HCHO (based on the QA4ECV NO_2 and HCHO dataset) as measured by OMI from October 2004 to March 2019, and include minimum spatial and temporal coverage thresholds (De Smedt et al., 2018). OMI has an overpass time of 13.30 local time and the retrieved column densities concern clear-sky or partially cloudy conditions.

2.2   IASI–SOFRID

The Software for a Fast Retrieval of Infrared Atmospheric Sounding Interferometer (IASI) data (SOFRID) retrieves global ozone profiles from IASI radiances (Barret et al., 2011, 2021). It is based on the RTTOV (Radiative Transfer for TOVS) operational radiative transfer model jointly developed by ECMWF, Meteo–France, UKMO and KNMI within the NWPSAF (Saunders et al., 1999; Matricardi et al., 2004). The RTTOV regression coefficients are based on line–by–line computations performed using the HITRAN2004 spectroscopic database (Rothman et al., 2005), and the land surface emissivity is computed with the RTTOV UW–

IRemis module (Borbas and Ruston, 2010). The IASI–SOFRID ozone for the study period (2008 to 2019) is obtained from METOP–A (2008-2018) and METOP–B (2019).

We use the SOFRID version 3.5 data presented and validated in Barret et al. (2021), which uses dynamical a priori profiles from an O_3 profile tropopause-based climatology according to tropopause height, month, and latitude (Sofieva et al., 2014). The use of such an a priori has largely improved the retrievals, especially in the SH where the previous version was biased. The retrievals are performed for clear-sky conditions (cloud cover fraction < 20%). IASI– SOFRID ozone retrievals provide independent pieces of information in the troposphere, the UTLS (300 – 150 hPa), and the stratosphere (150 – 25 hPa) (Barret et al., 2021). SOFRID TRCO absolute biases relative to ozonesondes are lower than 8 % with root mean square error (RMSE) values lower than 18 % across the six 30° latitude bands (see Barret et al. (2021)). Importantly, Barret et al. (2021) have shown that relative to ozonesondes, TRCO from IASI– SOFRID display no drifts (<2.1 % decade^{-1}) for latitudes lower than 60°N and in the SH for latitudes larger than 30° (<3.7 % decade^{-1}). But significant drifts are observed in the SH tropics (-5.2% decade^{-1}) and in the NH at high latitudes (12.8% decade^{-1}).

2.3   IASI+GOME2

IASI+GOME2 is a multispectral approach to retrieve the vertical profile of ozone and its abundance in several partial columns. It is based on the synergy of IASI and GOME2 spectral measurements in the thermal infrared and ultraviolet spectral regions, respectively, which are jointly used to improve the sensitivity of the retrieval for the lowest tropospheric ozone (below 3 km above sea level, see Cuesta et al., 2013). Studies over Europe and East Asia have shown particularly good capabilities for capturing near-surface ozone variability compared to surface in situ ozone measurements (Cuesta et al., 2018, 2022; Okamoto et al., 2023). TRCOs from IASI–GOME2 also show good agreement with several datasets of in-situ measurements for a four-year period in the tropics, with almost negligible biases and high correlations (Gaudel et al., 2024). This ozone product provides global coverage for low cloud fraction conditions (below 30%) for 12 km diameter pixels spaced 25 km apart (at nadir). The IASI–GOME2 global dataset is publicly available through the French AERIS data center, with data from 2017 to the present and covers the 90° S – 90° N latitude band. For this study, we use the monthly TRCO data between the surface and the tropopause for 2017 – 2019 for different latitude bands.

2.4   TROPOMI

The TROPOspheric Monitoring Instrument (TROPOMI) is the sole payload on the Copernicus Sentinel–5 Precursor (Sentinel–5P or S5P) satellite, which provides measurements of multiple atmospheric trace species, including NO_2 and HCHO, at high spatial and temporal resolutions (Veefkind et al., 2012). TROPOMI has a daily global coverage with a spatial resolution of 5.5 $\times$ 3.5 km^2 at nadir since a long-track pixel size reduction on 6 August 2019. We have used the ESA CCI+ Level–3 gridded 1° x 1° monthly tropospheric column of NO_2 (based on L2 v2.3.1, which applies a retrieval consistent with the most recent TROPOMI L2 version) and HCHO (https://doi.org/10.18758/2imqez32) (based on L2 v2.4.1, collection 3) data from May 2018 to December 2019 for our study (De Smedt et al., 2021; Glissenaar et al., 2024). This dataset waste created using the same methods as the ESA CCI+ OMI Level–3 datasets.

2.5   The ECHAM6-HAMMOZ model experiments

The ECHAM6.3–HAM2.3–MOZ1.0 aerosol chemistry–climate model (Schultz et al., 2018) used in the present study comprises the general circulation model ECHAM6 (Stevens et al., 2013), the tropospheric chemistry module, MOZ (Stevenson et al., 2006) and the aerosol module, Hamburg Aerosol Model (HAM) (Vignati et al., 2004). The gas phase chemistry is represented by the Jülich Atmospheric Mechanism (JAM) v002b mechanism (Schultz et al., 2018). This scheme is an update and an extension of terpenes and aromatics oxidation based on the MOZART–4 model (Emmons et al., 2010) chemical scheme. Tropospheric heterogeneous chemistry relevant to ozone is also included (Stadtler et al., 2018). MOZ uses the same chemical preprocessor as CAM–Chem (Lamarque et al., 2012) and WACCM (Kinnison et al., 2007) to generate a FORTRAN code containing the chemical solver for a specific chemical mechanism. Land surface processes are modelled with JSBACH (Reick et al., 2013). Biogenic VOC emissions are modelled with the MEGAN algorithm (Guenther et al., 2012) which has been coupled to JSBACH (Henrot et al., 2017). The lightning NOx emissions are parameterized in the ECHAM6–HAMMOZ as described by Rast et al. (2014). The lightning parameterization is the same in all the simulations. The model simulations were performed for the period 1998 to 2019 using the Atmospheric Chemistry and Climate Model Intercomparison Project (ACCMIP) (Lamarque et al., 2010; Van Vuuren et al., 2011) emission inventory. ACCMIP emission inventory includes emissions from agriculture and waste

burning, forest and grassland fires, aircraft, domestic fuel use, energy generation including fossil fuel extraction, industry, ship traffic, solvent use, transportation, and waste management. The model was run at a T63 spectral resolution corresponding to about $1.8° \times 1.8°$ in the horizontal dimension and 47 vertical hybrid σ – p levels from the surface up to 0.001 hPa. The details of model parameterizations and validation are described by (Fadnavis et al., 2019b, 2019a, 2021b, 2021a, 2022, 2023). We performed five experiments: (1) control (CTL) and four emission sensitivity experiments: (2) doubling anthropogenic emission of NOx globally (DoubNOx), (3) reducing anthropogenic emissions of NOx by 50 % globally (HalfNOx), (4) doubling anthropogenic emissions of all VOCs globally (DoubVOC), (5) reducing anthropogenic emissions of all VOCs by 50 % globally (HalfVOC). We performed each experiment from 1998 to 2019 after a spin-up of one year. We used the Representative Concentration Pathway (RCP) 8.5 high emission scenario (Van Vuuren et al., 2011) in all model simulations. In each experiment, the monthly varying AMIP–II sea surface temperature and sea ice representative of the period 1998–2019 were specified as a lower boundary condition. Anthropogenic VOC emissions included in the model are listed in the supplementary table S1.

TRCO is computed from the satellite data and model simulations by averaging O_3 amounts from the surface up to the tropopause. The partial tropospheric column is converted into a mixing ratio assuming a constant ozone mixing ratio in the troposphere. Tropopause considered is as described by the WMO thermal tropopause definition, the lowest level at which the temperature lapse rate decreases to 2 K km^{-1} or less (WMO, 1957). The estimated tropopause in the satellite data will show differences since the tropopause is quite variable in space and time; its location will depend on the employed reanalysis (e.g., Hoffmann and Spang, 2022). The vertical resolution of the satellite and the ECHAM6-HAMMOZ also affect the estimated tropopause. For comparison of the model with satellite datasets, e.g., IASI–SOFRID, OMI/MLS, we use model and satellite data for the same period.

2.6   Tropospheric ozone radiative effects

The tropospheric ozone radiative effect (TO3RE) is calculated as in Pope et al. (2024). While the radiative effect calculated in ECHAM6–HAMMOZ also includes impacts of aerosols and dynamical effects, here we isolate TO3RE by using the Rap et al. (2015) tropospheric ozone radiative kernel derived from the SOCRATES offline radiative transfer model (Edwards and

278 Slingo, 1996), including stratospheric temperature adjustments. To calculate the TO3RE, the

279 monthly averaged ECHAM6–HAMMOZ simulated ozone field is multiplied by the offline

280 radiative kernel (at every grid box). It is then summed from surface to the tropopause. The

281 simulated ozone data are mapped onto the spatial resolution of the radiative kernel and then

282 interpolated vertically onto its pressure grid. The equation for each grid box is

283 $TO3RE = \sum_{i=surf}^{trop} RK_i \times O_{3i} \times dp_i /100$ (1)

284 where TO3RE is the tropospheric ozone radiative effect (W m^{-2}), RK is the radiative kernel

285 (W m^{-2} ppbv^{-1} 100 hPa^{-1}), O_3 is the simulated ozone grid box value (ppbv), dp is the pressure

286 difference between vertical levels (hPa), and 'i' is the grid box index between the surface

287 pressure level and the tropopause pressure. The tropopause pressure is identified based on the

288 WMO lapse rate tropopause definition. Several past studies have used this approach of using

289 the SOCRATES offline radiative kernel with output from model simulations to derive the

290 TO3RE (Rap et al., 2015; Scott et al., 2018; Rowlinson et al., 2020; Pope et al., 2024).

291 **3. Results**

292 **3.1 Comparison of the simulated seasonal cycle in TRCO, NO₂ and HCHO with**
293 **satellites retrievals**

294 In this section, we compare the estimated TRCO from the model (CTL) simulation with

295 OMI/MLS (2005 – 2019), IASI–SOFRID (2008 – 2019), and IASI–GOME2 (2017 – 2019)

296 satellite retrievals. We compared simulated TRCO for the same period as individual satellite

297 retrievals. The comparison of monthly mean TRCO is made for 20° latitude bins in Figure 1.

298 In the northern tropics (0° N – 20° N) (Fig. 1a), the OMI/MLS data exhibits an annual cycle

299 with a peak in April, whereas the model indicates a peak in January. Both datasets show a

300 minimum in August. The model underestimates TRCO by 1.8 to 3.9 ppb during March to

301 October. In the 21° N – 40° N and 41° N – 60° N latitude bands (Fig. 1 b–c), the model shows

302 a one-month lead in the peak of the annual cycle compared to OMI/MLS. In the 21° N – 40°

303 N band, the model underestimates OMI/MLS TRCO by 2.8 – 6.1 ppb during the summer

304 months (May–August), while it overestimates TRCO by 4.1 – 8.3 ppb from October to March.

305 The 41° N – 60° N latitude band exhibits an underestimation in the model by 1.1 – 6.3 ppb

306 during June and July, while it overestimates (0.7 – 7.5 ppb) the rest of the year. In the Southern

307 Hemisphere (SH), OMI/MLS and the model show a similar pattern in the seasonal cycle. The

308 model shows a one-to-two-month lead in the annual cycle. However, the model shows an

309 underestimation of TRCO for all months. The model underestimates TRCO by 0.5 to 7.1 ppb

310 in the 0 – 20 °S, by 5.1– 15.3 ppb in 21° S – 40° S, and by 9.2 – 13.8 ppb in the 41° S – 60° S

311 latitude bands. The comparison of TRCO from IASI–SOFRID with the model shows features

312 similar to those in the OMI/MLS. In the 0° N – 20° N latitude band, the model underestimates

313 the TRCO by about 3.8 to 7.7 ppb from April to October and in the 21° N – 60° N latitude band

314 by 1.9 – 11.3 ppb in summer (May–August). In the SH, the model shows better agreement with

315 IASI–SOFRID than OMI/MLS. During the SH winter (June–August), the model overestimates

316 TRCO by 2.8 – 6.5 ppb in the latitude range of 0° S – 40° S. Conversely, it underestimates

317 TRCO by 2.7 – 8.2 ppb in the 41° S – 60° S throughout the year, which is less compared to

318 other satellite datasets. IASI–SOFRID is known to suffer from negative drifts in the SH (Barret

319 et al., 2021).

320 Interestingly, the model exhibits a fair agreement with IASI–GOME2 retrieved TRCO during

321 the summer months (May–August) in the Northern Hemisphere (NH). During the winter

322 months, the estimated TRCO shows a large overestimation of 8.3 – 11.7 ppb in the NH (0° N

323 – 40° N), while it is underestimated by 8.3 – 11.7 ppb in the 41° N – 60° N. In the SH, a fairly

324 good agreement is observed between the model and IASI–GOME2 TRCO, especially in the 0°

325 S – 40° S latitude band. The model overestimates the TRCO by 7.4 – 8.8 ppb in the 0° S – 20°

326 S during SH winter and underestimates by 4.7 – 6.7 ppb in the 21° S – 40° S belt during SH

327 summer (December–January–February). An overall underestimation of about 7 – 11.2 ppb in

328 TRCO is noted in the 41° S – 60° S throughout the year. Figure 1 shows that a peak in the

329 seasonal cycle in the model is earlier than the three satellite data between 40° N and 40° S. In

330 general, the model underestimates TRCO in summer in the NH and overestimates in winter

331 relative to OMI/MLS, and IASI–SOFRID. In the SH, the model underestimates TRCO

332 throughout the year compared to OMI/MLS, IASI–SOFRID, and IASI–GOME2, especially in

333 the 41° N – 60° N band. Although the model–satellite comparison is done for the same period,

334 the differences in sampling between the model and satellite measurements may cause the

335 observed differences. It should be noted that the spatial resolution, coverage, and diurnal

336 sampling time differ among the satellites which also contribute to the observed differences

337 among them.

338

339

340

341

342

343

344

345

346

347

348

349

350

351
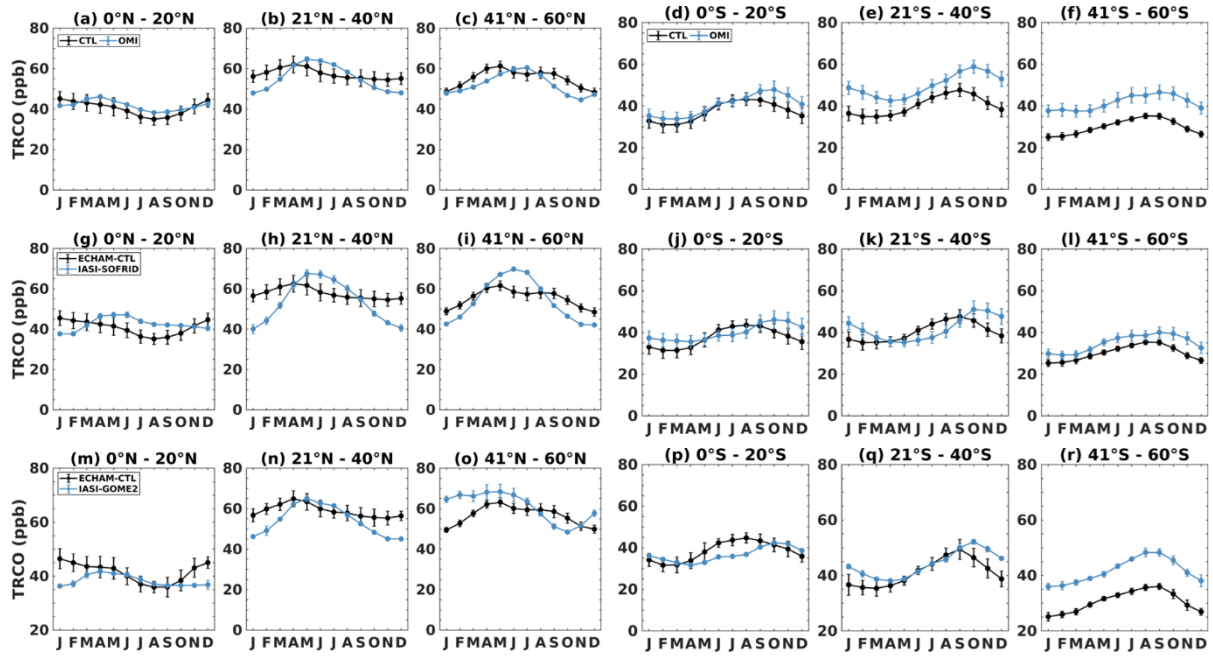
352 Figure 1. Time series of monthly mean TRCO (ppb) averaged for 20° wide latitude bins from
353 (a–f) OMI/MLS (blue) and ECHAM6–HAMMOZ CTL simulations (black) for the time period
354 October 2004 – December 2019. (g–l) same as (a–f) but for IASI–SOFRID (blue) and
355 ECHAM6–HAMMOZ CTL simulations (black) for the period January 2008 – December 2019,
356 and (m–r) same as (a–f) but for IASI–GOME2 (blue) and ECHAM6–HAMMOZ CTL
357 simulations (black) for the time period January 2017 – December 2019. The vertical bars in all
358 the figures represent 2σ standard deviation.

359

360 To evaluate our model simulations of NO_2 and HCHO, we compare the simulated tropospheric
361 column NO_2 and HCHO with the ESA CCI+ monthly averaged TROPOMI and OMI data (Fig.
362 2). The simulated NO_2 reproduces the seasonal cycle but shows overestimation in the entire
363 latitude band except 41° S – 60° S in the SH. In the NH, the magnitude of overestimation in
364 the simulated NO_2 increases with latitude. Simulated NO_2 is overestimated by 0.15 to 0.35
365 $\times 10^{15}$ molecules cm^{-2} in 0° N – 20° N, by 0.3 to 0.6 $\times 10^{15}$ molecules cm^{-2} in 21° N – 40° N,
366 and by 0.25 to 0.9 $\times 10^{15}$ molecules cm^{-2} in 41° N – 60° N latitude bands compared to
367 TROPOMI. Similarly, simulated NO_2 is overestimated compared to OMI by 0.16 to 0.35 $\times 10^{15}$
368 molecules cm^{-2} in 0° N – 20° N, by 0.16 to 0.48 $\times 10^{15}$ molecules cm^{-2} in 21° N – 40° N, and
369 by 0.18 to 0.76 $\times 10^{15}$ molecules cm^{-2} in 41° N – 60° N latitude belt (Fig. 2a–c and 2g–i).
370 Although the model overestimates NO_2 in the SH, the magnitude of this overestimation is
371 smaller compared to NH. Simulated NO_2 shows a fairly good agreement from 21° S to 60° S
372 latitudes in the SH (Fig. 2d–f and 2j–l).

373
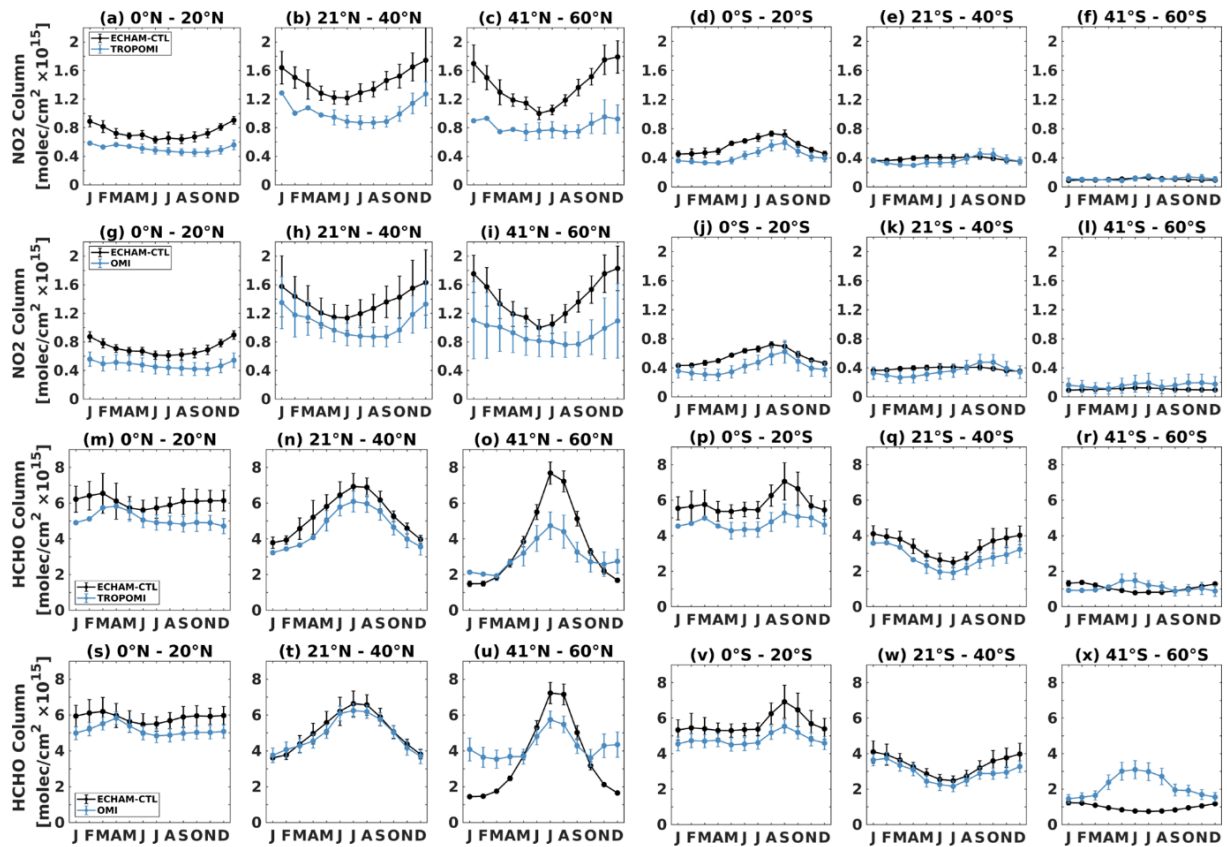
Figure 2. Time series of monthly mean tropospheric column NO_2 (molecules/cm^2) averaged for 20° wide latitude bins from ECHAM6–HAMMOZ CTL simulations (black) for the time period same as (a–f) TROPOMI from May 2018 to December 2019, and (g–l) OMI from January 2005 to December 2019. (m–x) are the same as that of (a–l) but for HCHO. The vertical bars in the figures represent 2σ standard deviation.

While the simulated HCHO successfully reproduces the seasonal cycle in both hemispheres, it shows a large overestimation, particularly in the tropical region (Fig. 2m–x). The overestimation is most pronounced when compared to TROPOMI, especially in the tropics, and to a lesser extent with OMI. The model HCHO aligns reasonably well with both TROPOMI and OMI in the northern and southern mid-latitudes (21° N – 40° N and 21° S – 40° S) with a modest overestimation of $0.4 – 1.2 \times 10^{15}$ molecules cm^{-2} and $0.3 – 0.5 \times 10^{15}$ molecules cm^{-2} respectively in the NH and $0.4 – 1 \times 10^{15}$ molecules cm^{-2} and $0.5 – 1.4 \times 10^{15}$ molecules cm^{-2} respectively in the SH. However, in the 41° N – 60° N band, the model overestimates HCHO compared to TROPOMI (OMI) by $0.6 – 2.9$ ($0.5–1.7$) $\times 10^{15}$ molecules cm^{-2} during the NH from May to October and underestimates it by $0.08 – 1.1$ ($0.01 – 2.7$) $\times 10^{15}$ molecules cm^{-2} during other months. On the contrary, the model underestimates HCHO in the 41° S – 60° S

during SH winter. It should be noted that TROPOMI/OMI monthly means are valid for clear-sky situations, whereas the model simulations are all-day all-sky averages. In previous studies (Boersma et al. (2016) and references therein), it was shown that NO_2 is typically 15 – 20 % lower on clear-sky days than under cloudy situations due to higher photolysis rates, and faster chemical loss of NO_2. Further, OMI and TROPOMI cannot sample for snowy scenes, and nighttime. There is significantly lower coverage on the NH during winter and vice versa for SH. These all can likely cause model and satellite differences. For HCHO the effect is smaller because HCHO is both produced and destroyed by OH (see Fig. 4 in Boersma et al. 2016). Considering these differences, we proceed with the analysis of TRCO trends, ozone photochemical regimes, and ozone radiative effects.

3.2. Impacts of emission changes on the spatial distribution of ozone

Figure 3 shows the spatial distribution of the simulated surface (Fig. 3a–e) and TRCO (Fig. 3f–j) concentration from ECHAM CTL simulations and the anomalies obtained from differences in DoubNOx - CTL, DoubVOC - CTL, HalfNOx - CTL, and HalfVOC - CTL simulations for the period 1998 – 2019. The CTL simulation shows high surface ozone levels (19 – 61.1 ppb) between 10° N – 40° N (Fig. 3a). Doubling of NOx emission (DoubNOx) causes a global mean enhancement of surface ozone anomalies by 4.1 [-3.8 to 13], [5th to 95th percentile] ppb. Surface ozone anomalies show an increase of 5 – 20 ppb across most of the globe, excluding highly urbanized regions like the Indo-Gangetic plains (IGP), Southeast China, Northeastern United States (US), and Europe. (Fig. 3b). Over these regions, a large reduction (8 – 20 ppb) in surface ozone anomalies is noticed, indicating ozone titration by NOx. While surface ozone anomalies from DoubVOC - CTL simulations show global mean enhancement by 0.9 [0.1 to 2.3] ppb, its magnitude is less than that of the anomalies from DoubNOx - CTL (Fig. 3c). The largest increase in surface ozone anomalies for DoubVOC is observed over IGP, Eastern China and the Eastern US (3 – 6 ppb). Interestingly, these are the same regions where a decrease in ozone anomalies is observed in the DoubNOx case. The decrease (increase) in ozone anomalies with an increase in NOx (VOC) emissions indicates that these regions could be NOx–saturated or VOC–limited. Reduction of NOx emissions (HalfNOx-CTL) simulations show a reduction in surface ozone anomalies (global mean by -2.5 [-7.2 to -0.7] ppb) except over North-Eastern China (Fig. 3d). Earlier, Souri et al. (2017) also reported that eastern Asia has witnessed a rise in surface ozone levels despite NOx control strategies, indicating the prevalence of VOC–

436 limited photochemistry over this region (details in section 4 to 6). However, the absence of

437 such an increase over other VOC–limited regions points towards nonlinear ozone chemistry.

438 While HalfVOC - CTL stimulation causes a reduction in surface ozone anomalies (global mean

439 -0.4 [-1.4 to 0.05] ppb), an increase is observed in South America, some parts of the US,

440 Australia, and the Indo-China peninsula (Fig. 3e). This increase could be due to a reduction in

441 the radical destruction of ozone caused by aromatic hydrocarbons in low NOx conditions in

442 these regions (Taraborrelli et al., 2021).

443

444 Further, we show the impact of emission changes on the TRCO distribution (Fig. 3f–j). The

445 estimated global mean TRCO from the CTL simulation from 1998 to 2019 is 39.4 [23.8 to

446 56.8] ppb (Fig. 3f). CTL simulations show higher amounts of TRCO (40.9 to 68.8 ppb) in the

447 latitudinal band of 20° N to 40° N. These concentrations are pronounced over South and East

448 Asia, spanning from the Mediterranean region to eastern China (Fig. 3f). TRCO anomalies

449 from DoubNOx - CTL show enhancement by 11.7 [6.9 to 19.8] ppb (global mean) (Fig. 3g).

450 Between 20° N – 40° N belt, the TRCO anomalies exceeds by 6.1 – 29.3 ppb, particularly over

451 South Asia. Interestingly, in highly urbanized areas such as the IGP, Southeast China,

452 Northeast US, and Europe, there is only a marginal increase in TRCO anomalies (~5 ppb). This

453 suggests the existence of a distinct ozone photochemical regime in these regions. Further

454 exploration of this aspect will be discussed in sections 4 to 6.

455 The impact of the doubling of VOC emissions (anomalies from DoubVOC - CTL simulations)

456 on TRCO is depicted in Figure 3h. An increase in global mean TRCO by 1 [-0.2 to 2.4] ppb is

457 observed in this emission scenario. It should be noted that TRCO anomalies from DoubVOC -

458 CTL are ten times less than that from DoubNOx - CTL (Fig. 3g and 3h). Large values of TRCO

459 anomalies (1.5 – 2) are observed in the high latitudes (north of 60° N) and South and East Asia,

460 with the largest values of more than 2.5 ppb over East China (e.g., Beijing). Interestingly, slight

461 decreases in TRCO are seen in the tropical regions. This is consistent with the recent finding

462 that aromatics, especially benzene, can lead to efficient ozone destruction in tropical UTLS

463 (Rosanka et al., 2021). The TRCO anomalies in response to the reduction of NOx emission by

464 50% (HalfNOx - CTL) show negative TRCO anomalies all over the globe (Fig. 3i). The global

465 mean TRCO anomalies are reduced by -3.7 [-7.9 to -1.1] ppb. Large decreases in TRCO

466 anomalies are seen over Arabia, South and East Asian regions (2.6 – 12.8 ppb). The TRCO

467 anomalies from HalfVOC - CTL show an overall decrease in TRCO by -0.27 [-0.97 to -0.4]

ppb (Fig. 3j). Further, a small enhancement is noted in the TRCO anomalies (by 0.5 – 1 ppb) in the southern tropics and south polar region, while a decrease of -2.3 to 0.3 ppb is observed in the NH. (Fig. 3j). Figure 3 clearly portrays that the TRCO response to NOx emission change is larger than that of VOCs. There is a spatially distinct distribution in TRCO associated with the region-specific ozone photochemical regimes (more discussion on the ozone photochemical regimes will be detailed in sections 4 – 6).
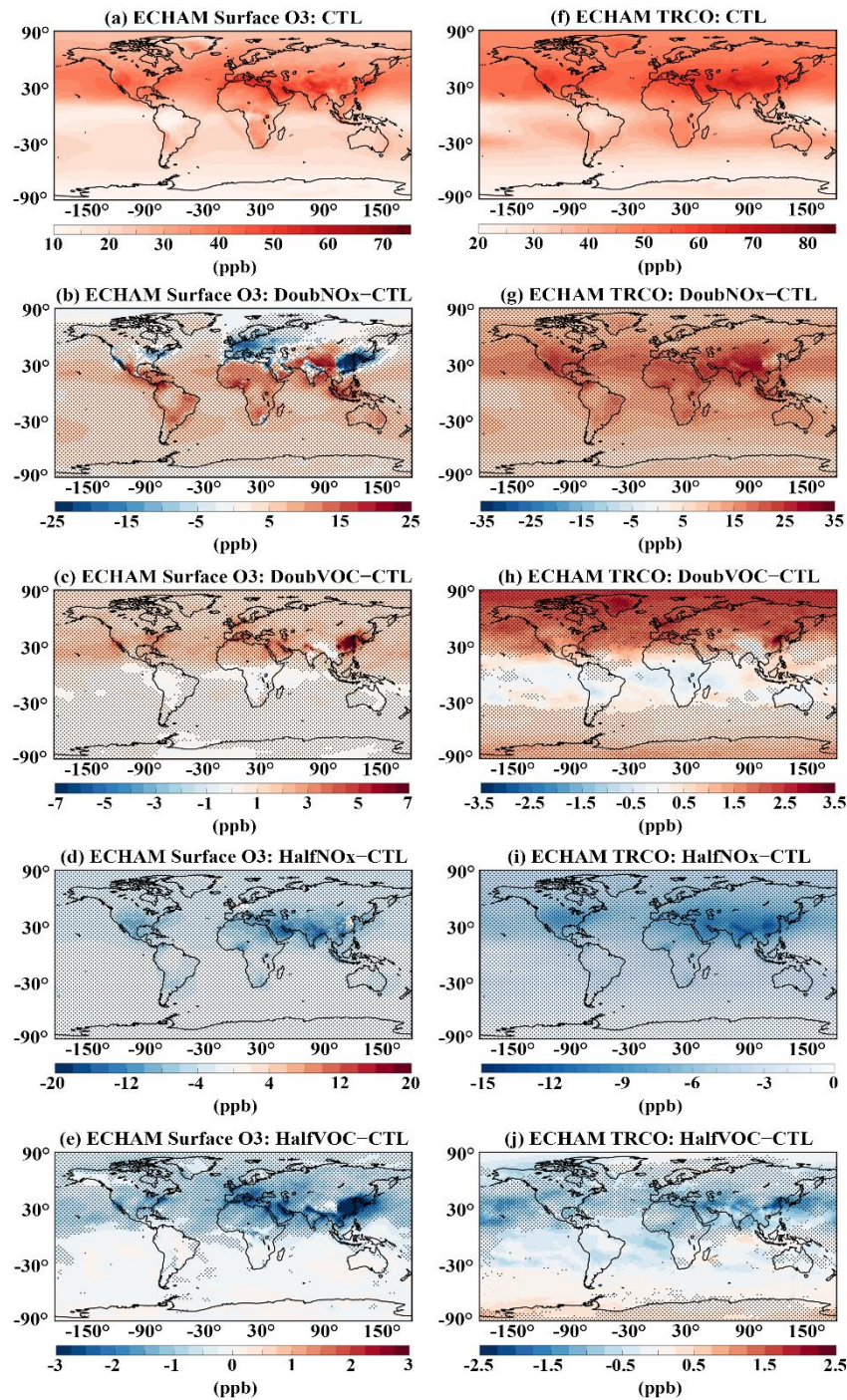
Figure 3. Spatial distribution of surface ozone (ppb) for (a) from CTL simulations, anomalies from (b) DoubNOx - CTL, (c) DoubVOC - CTL, (d) HalfNOx - CTL, and (e) HalfVOC - CTL simulations. (f–j) are the same as that of (a–e) but for TRCO. The stippled regions in the figures indicate anomalies significant at 95% confidence based on the t-test.

3.3. Spatial distribution of trends in ozone

We estimate trends in TRCO from ECHAM CTL simulations (1998–2019) and OMI/MLS satellite retrievals (2005–2019). The simulated trends are compared with satellite retrieves for the period 2005–2019. Since IASI–GOME2 has a short observation period (2017–2019) and IASI–SOFRID has negative drift in the SH, only TRCO from OMI/MLS is considered for trend estimation (Fig. 4). The spatial pattern of trends from OMI/MLS shows fair agreement with model simulations (Fig 4a-b). Quantitatively, the global mean TRCO trend from OMI/MLS is slightly lower than the model (OMI/MLS:1.43 [-0.5 to 3.2] ppb decade^{-1}; ECHAM-CTL: 1.58 [0.3 to 3.3] ppb decade^{-1}). Both datasets reveal high trends, ranging from 3–4 ppb decade^{-1}, across regions such as South Asia, East Asia, and the West Pacific. OMI/MLS show negative trends over parts of Africa, South America, Australia, and the southeastern Pacific (Fig. 4b), which is not simulated in ECHAM6–HAMMOZ. Although there is fair agreement in spatial patterns of TRCO trends between OMI/MLS and the model, the minor differences may be due to the model's tendency to underestimate ozone levels and differences in the seasonal cycle. (See Fig. 1).

TRCO trends analyzed from the Total Ozone Mapping Spectrometer (TOMS) indicate a consistent absence of trend over the tropical Pacific Ocean, with notable positive trends (4 – 5% decade^{-1}) seen in the mid-latitude Pacific regions of both hemispheres (Ziemke et al., 2005). This pattern is consistent across the ECHAM6–HAMMOZ and OMI/MLS data, although their magnitude differs (Fig. 4 a–b). TOMS data also showed trends of ~2 – 5% decade^{-1} across broad regions of the tropical South Atlantic, India, Southeast Asia, Indonesia, and the tropical/subtropical regions of China during 1979 – 2003 (Ziemke et al., 2005; Beig and Singh, 2007) which are also simulated in the model. Further, a large positive trend of ~2.5 ppb decade^{-1} observed near 50° S in OMI/MLS is not simulated by the model (Fig. 4a–b). The CESM2–WACCAM6 simulation from 1950 to 2014 also shows the largest trend estimate of 0.8 Tg decade^{-1} over 20° N – 30° N (Fiore et al., 2022). Large TRCO trends over 20° N – 30° N are also seen in OMI/MLS and the model (Fig.4). Wang et al. (2021) reported TRCO trends varying

528 between 2.55 to 5.53 ppb decade^{-1} during 19595–2017 over South and East Asia using IAGOS,

529 ozonesonde observations, and Goddard Earth Observing System–chemistry model (GEOS–

530 Chem). Our model also shows similar increasing trends.
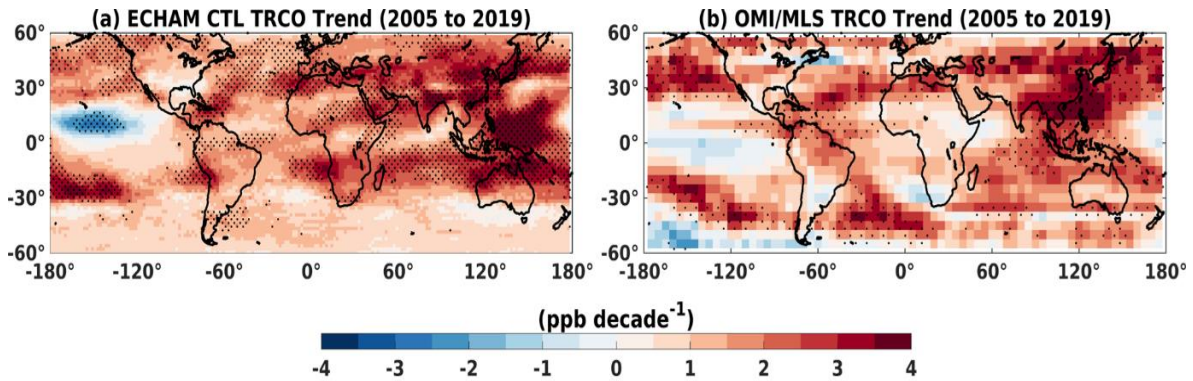
537 Figure 4. Trend of TRCO (ppb decade^{-1}) from (a) ECHAM CTL, and (b) OMI/MLS satellite
538 for the period January 2005 to December 2020. Stippled regions in the figures indicate trends
539 significant at 95% confidence based on the t-test.

541 Figure 5 shows the spatial distribution of estimated trends in surface ozone and TRCO

542 from CTL simulation for the period 1998 – 2019. Changes (Doubling/halving) in the emission

543 of NOx and VOCs will change ozone trends. Hence, we also analyzed anomalies in ozone from

544 DoubNOx - CTL, DoubVOC - CTL, HalfNOx - CTL, and HalfVOC - CTL. The surface ozone

545 trend in the CTL simulation shows spatial variation with a pronounced increasing trend over

546 South Asia and the Middle East (3 – 4 ppb decade^{-1}) (Fig. 5a). Similar pronounced increase is

547 also seen in the TRCO trend (Fig. 5b). The estimated global mean TRCO trend from CTL is

548 0.89 [-0.07 to 2.1] ppb decade^{-1}. However, the negative trends in surface ozone over Mexico,

549 certain parts of the US, and East China are barely discernible in the TRCO data. This

550 discrepancy may stem from the interplay of mixing and transport processes, stratospheric

551 intrusions, which are crucial when assessing ozone levels across the tropospheric column. The

552 stratospheric ozone intrusions lead enhancement in the tropospheric ozone (Prather and Zhu,

553 2024).

555 Figure 5 c–d shows trend in surface ozone and TRCO estimated from anomalies

556 obtained from DoubNOx - CTL simulations in the surface ozone and TRCO. A striking feature

557 is large negative trend anomalies over India and China at the surface (-4.8 to -8 ppb decade^{-1})

558 and TRCO (-2 to -4 ppb decade^{-1}). Whereas Europe, the US, some parts of Africa and South

559 America show positive trends at the surface (1.8 to 8 ppb decade^{-1}) and TRCO (2 to 4 8 ppb

560 decade^{-1}). The global mean ~~anomalies of the~~ TRCO trend are 1.2 [-0.1 to 2.7] ppb decade^{-1}.

561 ~~The high TRCO trends (1 – 3 ppb decade^{-1}) in the North of 60° N are seen in for all the~~

562 ~~sensitivity simulations. This may be due to transport and stratospheric intrusion in response to~~

563 ~~emission perturbation that affects the radiative forcing and dynamics (e.g., Fig. 5d, f, h, j).~~

564

565 When global emissions of VOCs are doubled, the trend in ozone estimated from

566 anomalies (DoubVOC - CTL) ~~in trends show~~ shows a decrease (by -0.8 to -1.9 ppb decade^{-1})

567 in surface ozone over Europe, Africa and some parts of the US, while strong positive trend

568 ~~anomalies~~ (1.6 to 2 ppb decade^{-1}) are seen over India and China (Fig. 5e). ~~Anomalies in~~ TRCO

569 trends show an enhancement over South Asia, Southwest Asia, China, parts of the Indian

570 Ocean, and the western Pacific (0.8 to 1.6 ppb decade^{-1}) (Fig. 5f). A global mean TRCO trend

571 ~~anomaly~~ for DoubVOC-CTL simulation is 0.5 [-0.03 to 1.04] ppb decade^{-1}. The estimated

572 enhancement in global mean TRCO trend ~~anomalies~~ for DoubVOC is less than DoubNOx

573 simulations. Figures 5 c and e also give indications of the existence of distinct ozone

574 photochemical regimes globally. The increasing (decreasing) trend in surface ozone with an

575 increase in VOC (NOx) over India and China indicates that these regions are in a VOC–limited

576 regime, and vice-versa over the US and Europe indicates that these regions are in a NOx–

577 limited regime (more discussions on sections 4 to 6).

578

579 Figure 5g–h shows the trend in surface and TRCO ozone estimated from anomalies

580 from HalfNOx - CTL. The surface ozone trend shows a large negative trend over Europe and

581 South Asia, while a positive trend over the US, China, and Australia (Fig. 5g). Trends in TRCO

582 also show a large negative trend over South Asia (Fig. 5h). Although anthropogenic NOx

583 emissions are halved compared to CTL, ~~The~~ ozone trends are positive over large region

584 globally ~~although anthropogenic NOx emissions are halved than CTL~~. Our investigations

585 reveal that the trend in~~from~~ VOC anomalies ~~of VOCs in~~from the HalfNOx-CTL simulations is

586 positive over the US, India, and Europe, while negative over China. Similarly, the trend in NOx

587 ~~from~~ anomalies ~~of NOx in~~from the HalfNOx-CTL simulations is positive over the US and

588 Europe while negative over India and China (Fig. S1a-b). It should be noted that over the US

589 and Europe the positive NOx trend estimated from anomalies (HalfNOx-CTL) suggests that

590 NOx levels in HalfNOx are declining more slowly compared to CTL, leading to relatively

higher NOx concentrations over time. While over India and China in NOx level is weak in HalfNOx compared to CTL, leading to a negative trend estimated from NOx anomalies (HalfNOx-CTL).

It is known that ozone response is non-linear to NOx and VOC emission changes and depending on the local photochemical regime. In the US, estimated trends from anomalies are positive in VOC and NOx (HALFNOX-CTL). This indicates that relatively more ozone precursors in the HalfNOx contribute to the observed positive ozone trend. Over Europe, the strong positive trend estimated from NOx anomalies (compared to VOCs) enhances NOx titration effects, contributing to the observed negative ozone trend. ~~The strong positive trend in both VOC and NOx might have resulted in the observed positive trend in surface ozone over the US, while the strong positive trend in NOx compared to that of VOCs over Europe might have resulted in more NOx titration effect causing the observed negative trend in ozone~~. China, being a VOC–limited regime, experiences reduced NOx titration under lower NOx conditions~~the reduction in NOx can decrease the NOx titration~~, resulting in positive ozone trends. Over India, the positive trend in VOC anomalies with a negative trend in NOx anomalies may enhance the radical destruction of ozone caused by aromatic hydrocarbons in low NOx conditions (Taraborrelli et al., 2021), resulting in a negative ozone trend. ~~Thus, f~~For HalfNOx – CTL, the global mean trend ~~anomaly~~ is positive 0.47 [-0.76 to 1.3] ppb decade^{-1}.

The trend in surface and TRCO ozone estimated from anomalies from HalfVOC – CTL is shown in Figure 5i-j. A large negative trend in surface ozone is noted over IGP and China, while an insignificant positive trend is noted over the US and Europe (Fig. 5i). The TRCO trend ~~anomalies~~ are positive over large regions in the world with pronounced high over the mid- and high latitudes although emissions of all anthropogenic VOCs are halved (Fig. 5j). The global mean trend ~~anomaly~~ for HalfVOC - CTL is 0.37 [-0.35 to 1.02] ppb decade^{-1}. Our analysis shows that the trend in NO_X anomalies and VOC anomalies from HalfVOC - CTL is decreasing over both India and China (Fig S1c-d). The negative trend in precursors might have resulted in a negative trend in ozone over these regions. The absence of strong trends in TRCO (Fig. 5 b, d, f, h, j) similar to that at the surface (Fig. 5 a, c, e, g, i) in all the simulations indicates the potential contribution of transport in the troposphere and stratospheric intrusions in TRCO. Ozone injection through stratosphere–troposphere exchange is important source of tropospheric ozone (Prather and Zhu, 2024).
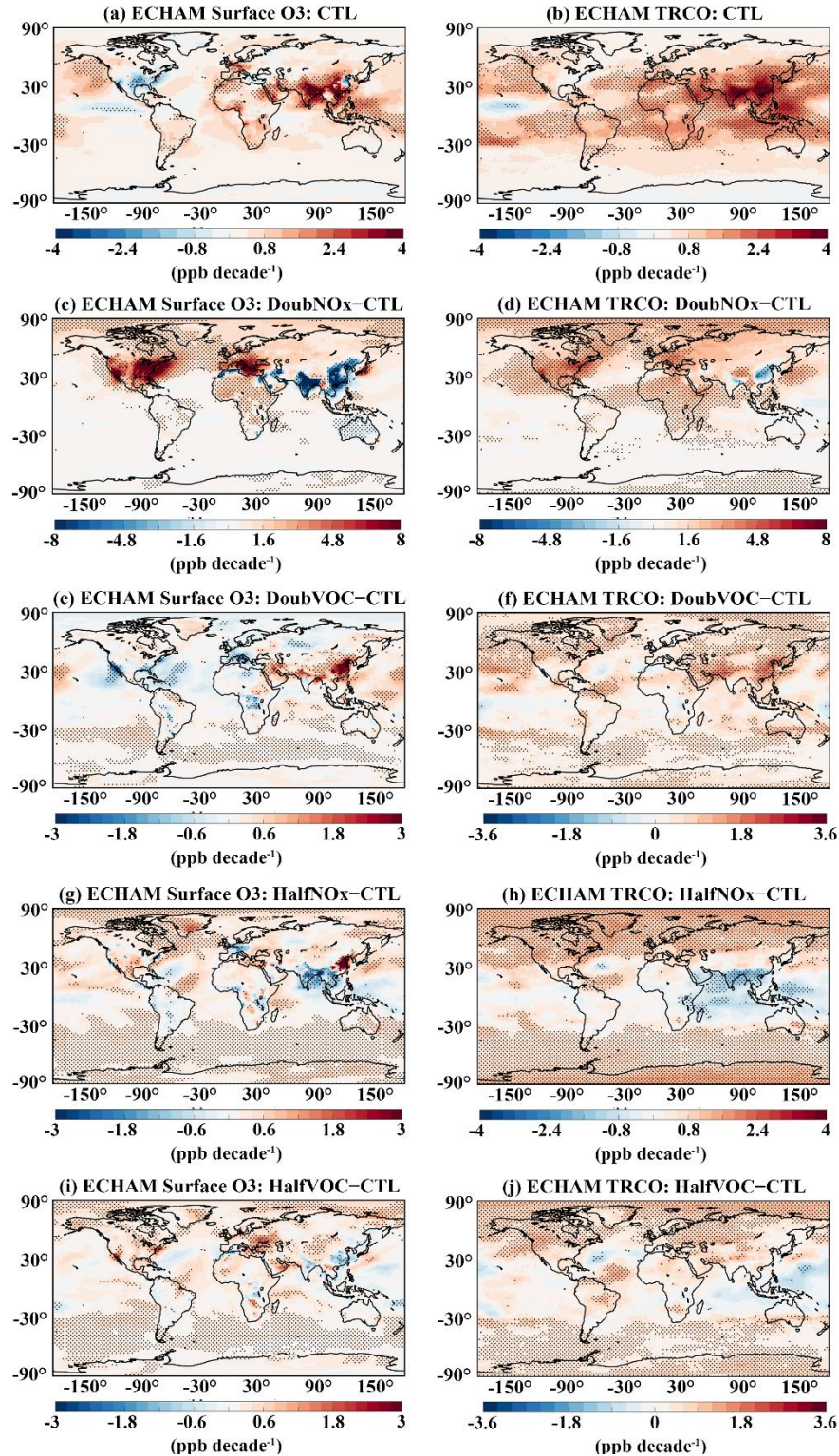
Figure 5. Trend in surface ozone (ppb decade^{-1}) for the period 1998-2019, calculated from (a) CTL, ozone anomalies in (c) DoubNOx - CTL, (e) DoubVOC - CTL, (g) HalfNOx - CTL, and (i) HalfVOC - CTL simulations. Panels (b, d, f, h, and i) represents the corresponding trend in ~~are the same as that of the top row but for the~~ TRCO ~~trend~~. The stippled regions in the figures indicate significance at 95% confidence based on the t-test.

3.4. Trends in emission and tropospheric column of NO$_2$ and HCHO

We show mean emissions of NOx (NO+NO$_2$) and HCHO over urban/semi-urban regions; US, Brazil, Europe, Africa, India, China, and Australia in Figure 6. High emissions of VOCs and NOx in India and China are evident in Figure 6. Furthermore, VOCs emissions are noted to be higher than NOx over all the regions. They are higher by a factor of 3.3 in the US, 11.3 in Brazil, 4.8 in Europe, 10.5 in Africa, 10.8 in India, 6.1 in China, and 6.7 in Australia.
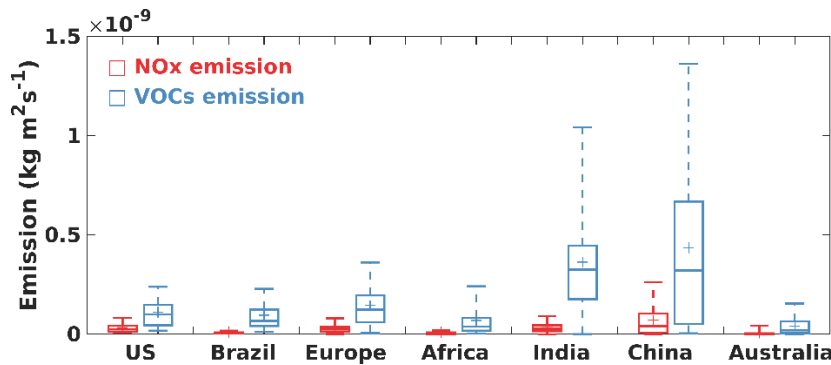
Figure 6. Box and whisker plot illustrating the NOx (NO+NO$_2$) and VOCs emission over the regions US (85°W – 110°W, 35°N – 44°N), Brazil (34°W – 49°W, 24°S – 3°S), European Union (9°W – 45°E, 35°N – 55°N), Central Africa (14°W – 45°E, 0° – 14°N), India (75°E – 90°E, 8°N – 30°N), China (110°E – 125°E, 30°N – 42°N), and South Australia (134°E – 154°E, 38°S – 28°S) from the ECHAM model. The box represents the 25 and 75 percentiles, and the whisker represents the 5 and 95 percentiles. The plus marker represents the mean, and the horizontal bar represents the 1 and 99 percentiles.

The trends in ozone are partly modulated by the change in the emission of its precursors and partly by meteorology (e.g., Verstraeten et al., 2015). We show trends in emissions and tropospheric column amounts of ozone precursors NO$_2$ and HCHO from ECHAM CTL and OMI satellite retrievals in Figure 7. NO$_2$ and HCHO are considered here because column densities of these will be used to identify the ozone photochemical regimes discussed later in Sections 4–6. Emissions and tropospheric columns of HCHO and NO$_2$ from ECHAM–CTL show large positive trends over the South and East Asian regions (Fig. 7a–d). These regions show large positive ozone trends in both model and OMI satellite data (see Fig. 4 and 5). Over Europe and the US, the emission trend in both HCHO and NO$_2$ from the model is negative (Fig. 7a, c). Though a similar negative trend in tropospheric column NO$_2$ is seen over these regions, a marginal positive trend is noted for HCHO (Fig. 7b, d). The positive trend in column HCHO could be due to secondary production pathways from biogenic emissions or methane oxidation and transport (e.g., Anderson et al., 2017; Alvarado et al., 2020). The positive trend

688 in ozone (Fig. 4a–b and 5a, f) along with a negative trend in NO_2 and HCHO (Fig. 7a–d) over

689 Europe indicates that ozone production over this region has been initially controlled by VOCs

690 (i.e., VOC–limited regime; detailed discussed in section 4). However, a large decreasing trend

691 in NO_2 compared to that of HCHO over this region might have decreased the NOx titration

692 effect, resulting in an increase in ozone. On the contrary, a negative trend in surface ozone (Fig.

693 5a) along with negative trends in NO_2 and HCHO are seen over the US (Fig. 7a–b). The

694 decrease in both NO_2 and HCHO would have resulted in a decreasing trend in surface ozone

695 over this region. This also indicates that the US might have been in a NOx–sensitive regime

696 before and the large negative trend in NO_2 might have resulted in the decreasing trend in ozone

697 (discussed further in section 4-6).

698

699 Further we compared the simulated trends in column HCHO and NO_2 with the OMI retrievals

700 for the period 2005–2019 (Fig. 7e–h). OMI shows a positive trend in tropospheric column

701 HCHO over South Asia $(1 - 1.5 \times 10^{15}$ molecules cm^{-2} decade^{-1}), parts of western China (0.75

702 $- 1.25 \times 10^{15}$ molecules cm^{-2} decade^{-1}), the Iranian Plateau $(0.5 - 1 \times 10^{15}$ molecules cm^{-2}

703 decade^{-1}), the Amazon $(1 - 1.5 \times 10^{15}$ molecules cm^{-2} decade^{-1}), North America (0.5 – 1.5

704 $\times 10^{15}$ molecules cm^{-2} decade^{-1}), Europe $(0.5 - 1 \times 10^{15}$ molecules cm^{-2} decade^{-1}), and central

705 Africa $(1 - 1.5 \times 10^{15}$ molecules cm^{-2} decade^{-1}). The model simulated trends show reasonable

706 agreement with OMI, except for western areas in central Africa, north Africa, southwest and

707 southeast China, and some parts of Australia. Over these regions OMI indicates a negative

708 trend, while the model suggests a marginal positive trend. OMI and ECHAM CTL show a good

709 agreement in the tropospheric column NO_2 trend. Both datasets show negative trends over the

710 eastern US and Europe, and positive trends over the Middle East, and South Asia. However,

711 differences are seen in eastern China and central Africa, where OMI indicates a negative trend,

712 while the model shows a strong positive trend. The differences between simulated and OMI

713 HCHO and NO_2 column trends may be due to sampling time and differences in seasonal cycle.

714 Figures 4, 5, and 7 clearly indicate the impact of ozone precursors on the spatial distribution of

715 ozone trends. This warrants a detailed discussion on the spatial distribution of ozone precursors

716 and their impact on ozone production-sensitive regimes, which will be presented in the next

717 section.

718

719
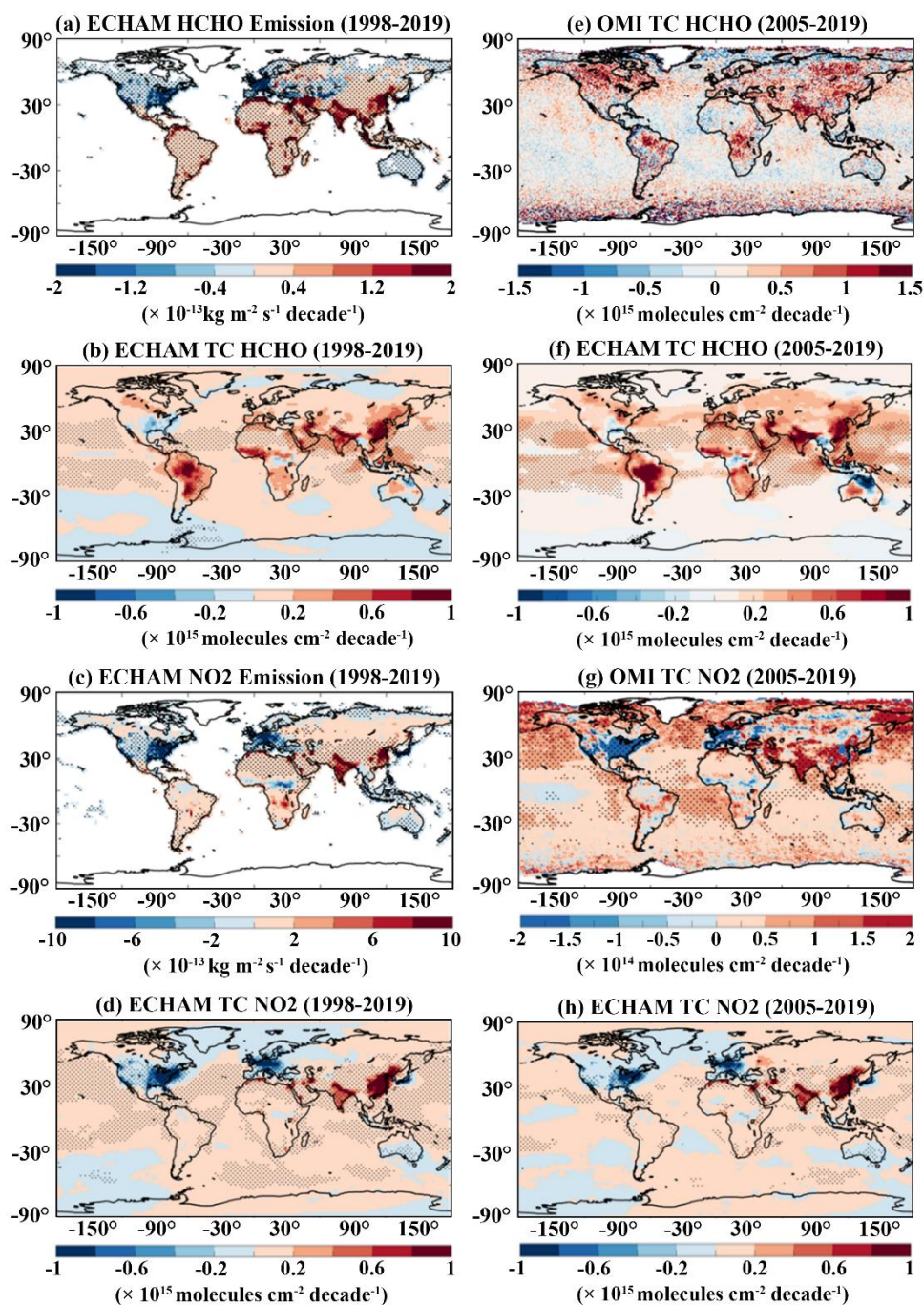
Figure 7. Trend in anthropogenic emission (kg m^2 s^{-1} decade^{-1}) from ECHAM CTL simulation for the period 1998–2019 for (a–b) HCHO and NO$_2$ respectively. Trends in tropospheric column (TC) (molecules cm^{-2} decade^{-1}) for (c–d) HCHO and NO$_2$ respectively. Trend in tropospheric column of HCHO from (e) OMI, and (f) ECHAM–CTL simulations for the period 2005-2019. (g–h) are the same as that of (e–f) but for tropospheric column NO$_2$. The stippled regions in the figures indicate significance at 95% confidence based on the t–test.

4. Influence of NOx and VOCs emissions on Formaldehyde to Nitrogen dioxide Ratio

In this section, we diagnosed the spatial distribution of tropospheric ozone production sensitivity regimes (NOx–limited/VOC–limited) associated with simulations of emission changes by using formaldehyde to nitrogen dioxide ratio (FNR). We estimate the FNR thresholds from ECHAM6–HAMMOZ model simulations adhering to the methodology outlined by Jin et al. (2017). The procedure to obtain FNR involves two steps: (1) obtaining the annual and seasonal ozone response from emission sensitivity simulations (here, HalfNOx and HalfVOC simulations) by considering only the polluted cells over the study region and plotting it as a function of FNR (Fig. 8a), (2) calculating cumulative probability from this data for the conditions $d[O_3]/dE_{NOx} < 0$) (~~NOx~~VOC limited) and ($d[O_3]/dE_{NOx} > d[O_3]/dE_{VOC} > 0$) (~~VOC~~NOx–limited) (Fig. 8b), where $d[O_3]/dE$ represents the change in ozone corresponding to a change in emission of either NOx or VOCs. This approach is applied to estimate seasonal and annual FNR thresholds to distinctly delineate the ozone photochemical regimes as NOx or VOC–limited over major urban and semi-urban regions. The regions considered for estimating the FNR are shown in Figure 9.
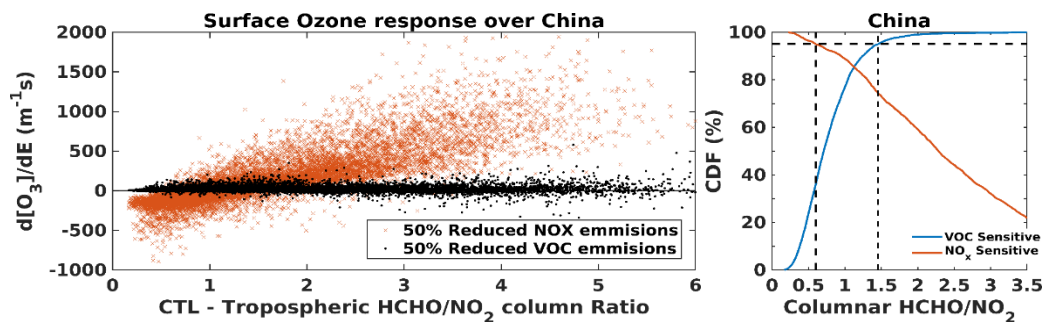
Figure 8. (a) Typical example of a normalized surface ozone sensitivity to a 50% reduction in global NOx (HalfNOx) and VOC (HalfVOC) emissions versus tropospheric column HCHO/NO₂ ratio derived from ECHAM6–HAMMOZ model simulation over China for the period 1998 – 2019, (b) Cumulative probability (CP) of VOC–sensitive ($d[O_3]/dE_{NOx} < 0$) and NOx–sensitive ($d[O_3]/dE_{NOx} > d[O_3]/dE_{VOC} > 0$) conditions, as a function of tropospheric column HCHO/NO₂ as simulated by the ECHAM6–HAMMOZ model. The horizontal dashed line represents the 95% CP, and the vertical dashed lines represent the HCHO/NO₂ ratio corresponding to 95% CP for both the VOC–sensitive and NOx–sensitive curves demarcating the VOC–sensitive, NOx–sensitive, and transition regimes.
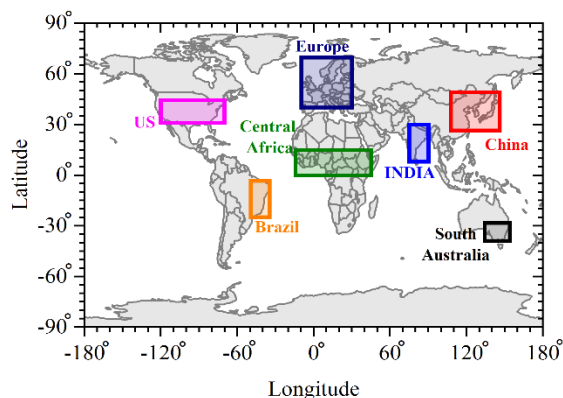
Figure 9. The rectangular box marks indicate the regions considered for estimating the HCHO/NO₂ ratio (FNR).

Table 3 presents FNR thresholds across the regions outlined in Figure 9. Based on ECHAM6–HAMMOZ simulations, our analysis closely mirrors the threshold ranges documented in prior research. For instance, during summer in the USA, many studies report FNR thresholds within the 0.8 – 2 range (Chang et al., 2016; Jin et al., 2017; Roberts et al., 2022), while our simulations indicate a range of 0.3 to 1.05. Similarly, across China, previous studies have reported FNR thresholds spanning 1 – 2 (Lee et al., 2022) and 0.6 – 3 (Chen et al., 2023), aligning closely with our simulated range of 0.6 – 1.45. It is interesting to note that the transition region exhibits a very narrower range in the US, Europe, and China, indicating that the transition from VOC–limited to NOx–limited can happen suddenly in response to changes in the emission of NOx/VOC. Whereas the transition region is wider in Central Africa.

Table 3. Estimated values of the tropospheric HCHO/NO₂ columns threshold ratios from ECHAM6–HAMMOZ model control simulation to identify the NOx and VOC sensitive regimes across various regions. The FNR less than the lower limit indicates VOC–limited, and that higher than the upper limit indicates NOx–limited regimes.

Sr. No.	Regions	Transition limits	
1	US (85° W – 110° W, 35° N– 44° N)	0.44	1.14
2	Brazil (34° W – 49° W, 24° S – 3° S)	3.04	7.53
3	European Union (9° W – 45° E, 35° N – 55° N)	0.3	1.37
4	Central Africa (14° W – 45° E, 0° – 14° N)	3.24	7.19
5	India (75° E – 90° E, 8° N – 30° N)	2.27	4.63
6	China (110° E – 125° E, 30° N – 42° N)	1.14	1.91
7	South Australia (134° E – 154° E, 38° S – 28° S)	1.03	3.28

828 Further, we compared the model-estimated FNR with the OMI-derived FNR for the period
829 2005 – 2019. Figure 10 illustrates the comparison of FNR estimated from ECHAM6–
830 HAMMOZ CTL simulations with OMI. The spatial map of FNR shows fairly good agreement
831 between OMI and the model. Over the urbanized regions (e.g., South Asia, Europe, the US,
832 and China) both the model and OMI show FNR < 4. In contrast, regions like North Canada,
833 South America, central Africa, Australia, and Siberia exhibit high FNR values >9. There is
834 good agreement between the model simulations and OMI, however, some minor differences
835 are seen between the model and OMI FNR over the west coast of South America, South Africa,
836 the Tibetan Plateau, and western Australia.
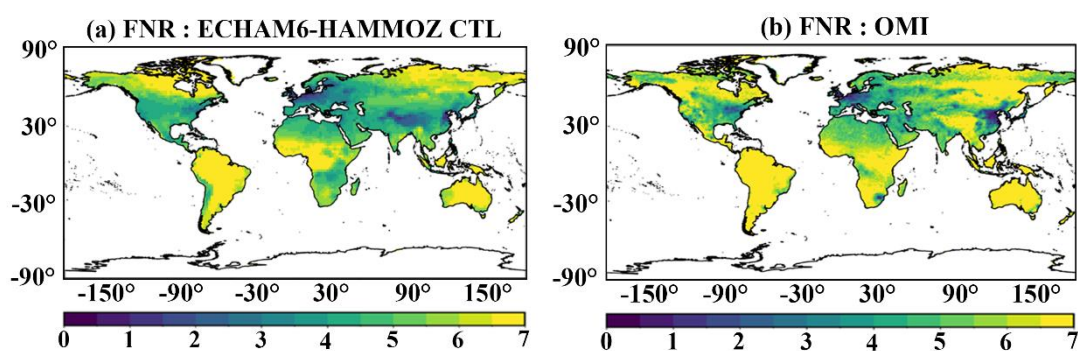
Figure 10. Spatial distribution of mean tropospheric column $HCHO/NO_2$ (FNR) obtained from
ECHAM6–HAMMOZ CTL simulations (2005 – 2019) and OMI (2005 – 2019).

846 These differences could be due to the underestimation of HCHO in the model over these
847 regions. Considering the fair performance of the model in comparison with OMI, we further
848 analyzed the influence of changes in NOx and VOC emissions on the FNR from the model
849 simulations, which are discussed in the subsequent sections.

851 Figure 11 shows the spatial distribution of FNRs estimated from CTL, DoubNOx,
852 DoubVOC, HalfNOx, and HalfVOC simulations. In the control simulation for the period 1998
853 – 2019, most of the polluted cities/industrialized areas in the US, Canada, Europe, west Russia,
854 East China, Korea and Japan are VOC limited (FNRs <2). The NOx–limited regimes (largest
855 FNR values >5) are found over the rural or unpolluted background regions like tropical
856 rainforest, savanna, and arid climates where biogenic emissions of VOCs are high (e.g., Millet
857 et al., 2008; Shen et al., 2019) (see Table 3 and central Africa in Fig. 11f). The DoubNOx

858 simulation yields a shift in the spatial extent of VOC-limited regimes (Fig. 11b). Regions across
859 the NH exhibit VOC–limited regimes, except central Africa, Amazonia, and north Australia.
860 Notably, the SH exhibits minimal change in the spatial extent of VOC–limited regimes with
861 consistent occurrences over the western coastlines of South America, Argentina, Brazil, South
862 Africa, and southern Australia.
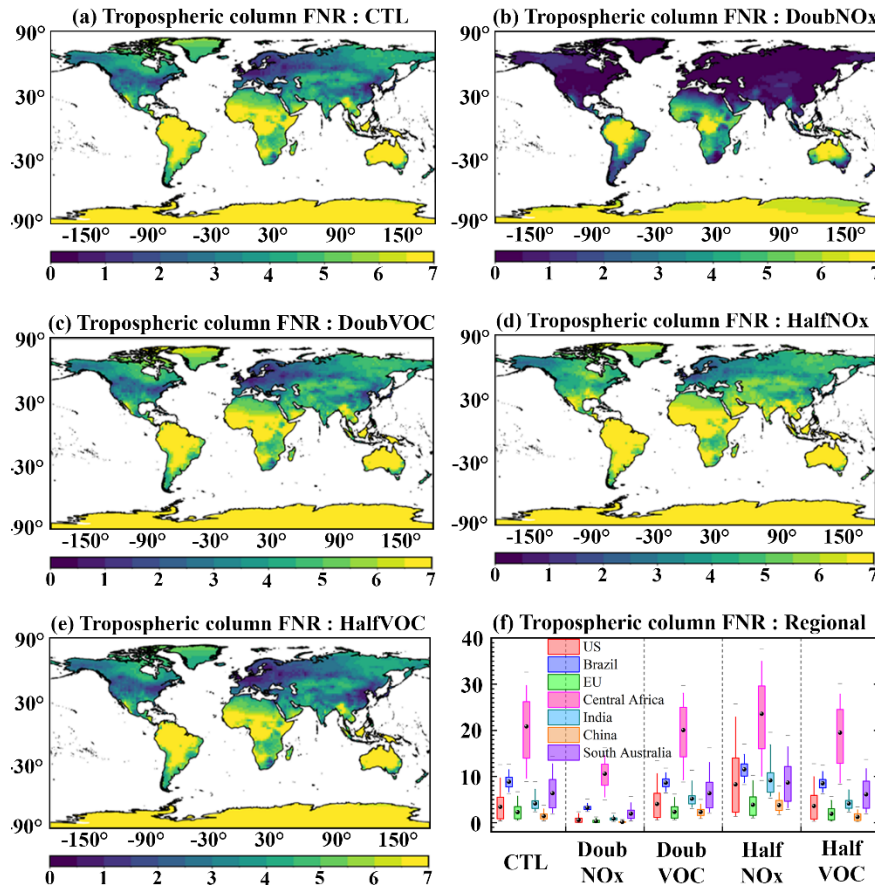
876 Figure 11. Spatial distribution of monthly mean tropospheric column HCHO/NO$_2$ (FNR)
877 obtained from ECHAM6–HAMMOZ simulations (1998 – 2019) for (a) CTL, (b) DoubNOx,
878 (c) DoubVOC, (d) HalfNOx, and (e) HalfVOC simulations. (f) Box and whisker plot
879 illustrating the long-term average FNR over the regions depicted in Fig. 9. Box represents 25
880 and 75 percentile and whisker represents 5 and 95 percentiles. The black spherical marker
881 represents the mean and the horizontal bar represents the 1 and 99 percentiles.

882 The DoubVOC simulations show (Fig. 11c) a persistent occurrence of VOC–limited regimes
883 over Western Europe (e.g., the UK). The moderate FNR values (1 – 6) prevail across most of
884 the NH, indicating a transition or NOx–limited regime. The spatial distribution of FNR in the
885 SH is similar to that of the control simulation. In Figure 3b–c, the increase in ozone in response
886 to a decrease in NOx and an increase in VOC is attributed to the existence of a VOC–limited
887 regime over these regions. The IGP, Eastern China and the eastern US clearly indicate the

888 VOC–limited condition. The comparison of CTL and HalfNOx simulation (Fig. 11d) shows
889 the transition from VOC–limited regimes to NOx–limited regimes occurring globally.
890 The FNR distribution for HalfVOC simulations is similar to CTL (as depicted in Fig. 11e)
891 without any notable change in the spatial pattern. This suggests that ozone photochemistry
892 exhibits less sensitivity to halved VOC emissions. Figure 11 clearly depicts that DoubNOx and
893 HalfNOx simulations greatly impact the shift in ozone photochemical regimes compared with
894 DoubVOC and HalfVOC simulations. This indicates that ozone photochemistry is highly
895 sensitive to changes in NOx emissions globally.

896

897 5. **Seasonal variation of Formaldehyde to Nitrogen dioxide Ratio**

898 Since the emission of HCHO and NO_2 varies with the seasons across the globe (e.g., De Smedt
899 et al., 2015; Wang et al., 2017; Surl et al., 2018; Kumar et al., 2020; Goldberg et al., 2021;
900 Guan et al., 2021), understanding the seasonal changes in FNR is also crucial for
901 comprehending shifts in ozone photochemical regimes. In this regard, using the methodology
902 described in Section 4, we extracted the seasonal changes in transition limits for the major
903 urban and semi-urban regions shown in Figure 9 and summarized in Table 4. Figure 12
904 illustrates the seasonal variation of estimated FNR from both OMI data and model simulations
905 across these key urban regions. In general, all regions exhibit distinct seasonal variations in
906 transition limits (Table 4). Previously reported transition limits over the US (2 – 5: Johnson et
907 al., 2024; 1.1 – 4: Schroeder et al., 2017) and China 0.6 – 1.5/1.25 – 2.39 (Chen et al., 2023)
908 during the summer season are also compared with our model estimates. The estimated FNR
909 values from the ECHAM6–HAMOZ simulations show fair agreement over both locations (0.4
910 – 4.6 in the US and 0.58 – 2.56 in China) with some minor differences. These minor
911 discrepancies in the estimated FNR could be due to differences in the chosen location, time
912 period and dataset used. Chen et al. (2023) have also reported that the transition limits depend
913 on the region considered for the analysis.

914

915 Based on the threshold values depicted in Table 4 and the mean FNR in Figure 12, the seasonal
916 change in ozone photochemical regimes over the key regions associated with the different
917 emission scenarios are assessed. In the CTL simulation (Fig. 12e – h), the US, Europe, and
918 China are found to be in the transition regime, while all other regions are NOx–limited during

919 winter. In spring every region except India remains NOx–limited, with India transitioning into
920 the transition regime. During summer and autumn, all regions shift to a NOx–limited condition.
921 We further compared the model-estimated regional FNR from the CTL simulation with the
922 OMI-derived FNR shown in Figure 12a – d. The ozone photochemical regimes inferred from
923 both OMI and the model show consistent results except during winter. During winter, the US,
924 Europe and China are NOx limited in OMI, while our model shows them in the transition
925 regimes.

926

927 Doubling NOx (DoubNOx) leads to a shift to a VOC–limited regime in all regions except
928 Africa and Australia during winter, spring, and autumn (Fig 12i – l). The relatively high VOC
929 contributions in Africa and Australia likely keep these regions in the transition regime. During
930 summer, the US, Europe, Africa and Australia transform to the transition regimes, while all
931 other regions remain VOC–limited. In both the DoubVOC and HalfNOx scenarios (Fig 12m –
932 t), ozone photochemical regimes show no seasonality. All regions consistently exhibit a NOx–
933 limited regime throughout all seasons. In the HalfVOC simulation (Figure 12u – x), the US,
934 Europe, and China are in transition regimes, while all other regions become NOx–limited
935 during winter. India remains in a transition regime during all other seasons, whereas other
936 regions consistently exhibit NOx–limited conditions.

937 Table 4. Seasonal mean estimated values of the tropospheric HCHO/NO$_2$ columns threshold
938 ratios from ECHAM6–HAMMOZ model control simulation to identify the NOx and VOC
939 sensitive regimes across regions mentioned in Figure 9. The FNR less than the lower limit
940 indicates VOC–limited, and that higher than the upper limit indicates NOx–limited regimes.

Sr. No.	Regions	Transition limits of FNR							
		DJF		MAM		JJA		SON	
1	US	0.48	1.04	0.49	1.15	0.49	4.69	0.45	1.39
2	Brazil	2.93	7.79	2.93	6.66	2.93	6.02	3.12	8.44
3	European Union	0.33	1.13	0.33	1.17	0.33	3.32	0.3	1.45
4	Central Africa	2.95	7.26	2.92	5.66	2.93	6.56	3.14	7.06
5	India	2.23	3.91	2.22	9.19	2.22	5.76	2.27	5.29
6	China	0.56	1.85	0.57	1.86	0.58	2.56	1.14	2.01
7	South Australia	1.1	5.54	1.09	2.3	1.09	1.82	1.12	3.93
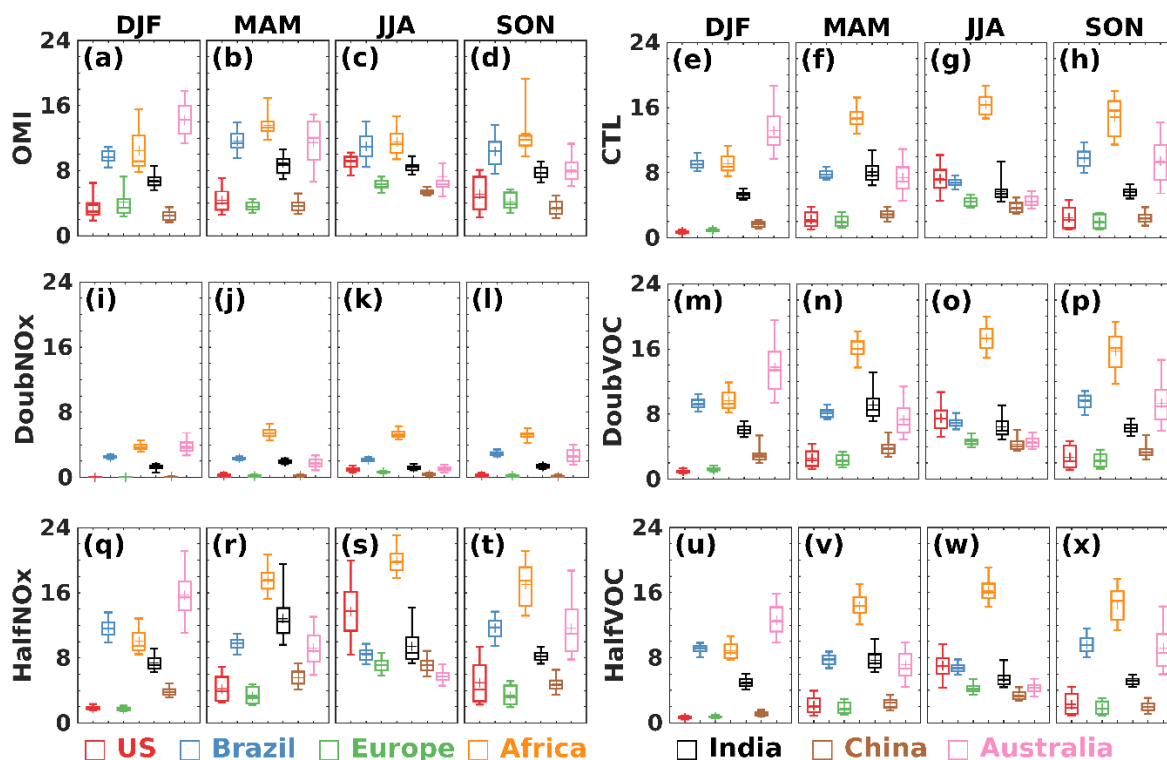
Figure 12. Box and whisker plot illustrating the long-term seasonal average FNR over the regions depicted in Fig.7 from (a-d) OMI observations, and model (e-h) CTL, (i-l) DoubNOx, (m-p) DoubVOC, (q-t) HalfNOx, and (u-x) HalfVOC simulations. Box represents 25 and 75 percentile and whisker represents 5 and 95 percentiles. The plus marker represents the mean, and the horizontal bar represents the 1 and 99 percentiles.

6. Influence of NOx and VOCs emissions on trends of Formaldehyde to Nitrogen dioxide Ratio

Trend analysis is carried out on FNR to understand the temporal evolution of ozone photochemical regimes associated with different emission scenarios. Figure 13 illustrates trends of FNR during the period 1998 – 2019 from CTL, DoubNOx, DoubVOC, HalfNOx, and HalfVOC simulations. In CTL simulation, decreasing (negative) trends in FNR are seen over the Asian region (-0.4 to -1.2 decade^{-1}) and Australia (-0.8 to -1.6 decade^{-1}), and an increasing (positive) trend in Europe (0.2 decade^{-1}) and the US (0.8 – 1.4 decade^{-1}) (Fig. 13a). These observed trends in FNR are mainly driven by the region-specific trends in HCHO and NO$_2$ (Fig. 7). Figure 7 shows a higher positive trend in NO$_2$ than in HCHO in the Asia region, causing an overall decreasing trend in FNR, indicating a tendency towards VOC–limited regimes. Whereas, over the US and Europe, there is a higher negative trend in NO$_2$ than HCHO, causing a positive trend in FNR, indicating a tendency towards a NOx–limited regime. A recent

983 study by Elshorbany et al. (2024) also reported a significant positive trend over Europe and the

984 US and a negative trend over Asia using the OMI-based tropospheric column HCHO/NO_2 ratio.

985 Further, long-term column measurements of HCHO and NO_2 from OMI over India and China

986 have revealed an increasing trend in NO_2 compared to that of HCHO, causing a decreasing

987 trend in FNR over these regions (Jin and Holloway, 2015; Mahajan et al., 2015).

988

989 DoubNOx simulation (Fig. 13b) shows a similar spatial trend pattern to that of CTL simulation

990 (Fig. 13a). However, the magnitude of this trend is less than that of the CTL. For example, a

991 weak positive trend is noted in the US and Europe (0.2 – 0.4 decade^{-1}), while trends over India,

992 and China are less negative (-0.2 to -0.4 decade^{-1}) in DoubNOx than CTL. (Fig. 13b). On the

993 contrary, the magnitude of the positive trend over Canada and the negative trend over central

994 Africa increased in DoubNOx emission, while the negative trend over Australia became

995 nominal and insignificant. This indicates that Canada and central Africa have a tendency to

996 become NOx–limited and VOC–limited respectively.

997 In DoubVOC simulations, trends are marginally increasing over the US, Canada, and Europe

998 compared to the CTL (Fig. 13a and 13c). A notable change is observed over the Middle East

999 and Amazon, where trends become more negative and positive respectively compared to CTL.

1000 The negative trends over Australia in the CTL become nominal and insignificant in the

1001 DoubVOC simulation. In HalfNOx simulations (Fig. 13d), the positive trends are higher over

1002 the US, Europe and Amazon, while negative trends prevail over India, China and northeast

1003 Australia. Meanwhile, in HalfVOC simulation, marginal changes are noted globally compared

1004 to CTL. The most pronounced change in the FNR trend is observed over West Australia, where

1005 the negative trend in CTL becomes positive in HalfVOC (Fig. 13e). Figure 13f clearly shows

1006 that the trend in FNR is always negative over India and China for all the simulations, indicating

1007 that these regions have a tendency to become VOC–limited, while the positive trends over

1008 Europe and US show a tendency to become more NOx–limited. Further, from Figures 5, 11

1009 and 13, we can infer that the relation between trends in FNR and ozone exhibits a nonlinearity.

1010 For example, even though FNR shows a negative trend over India and China for all the

1011 simulations, the TRCO trend depends on the specific emission scenario.

1012

1013

1014

1015
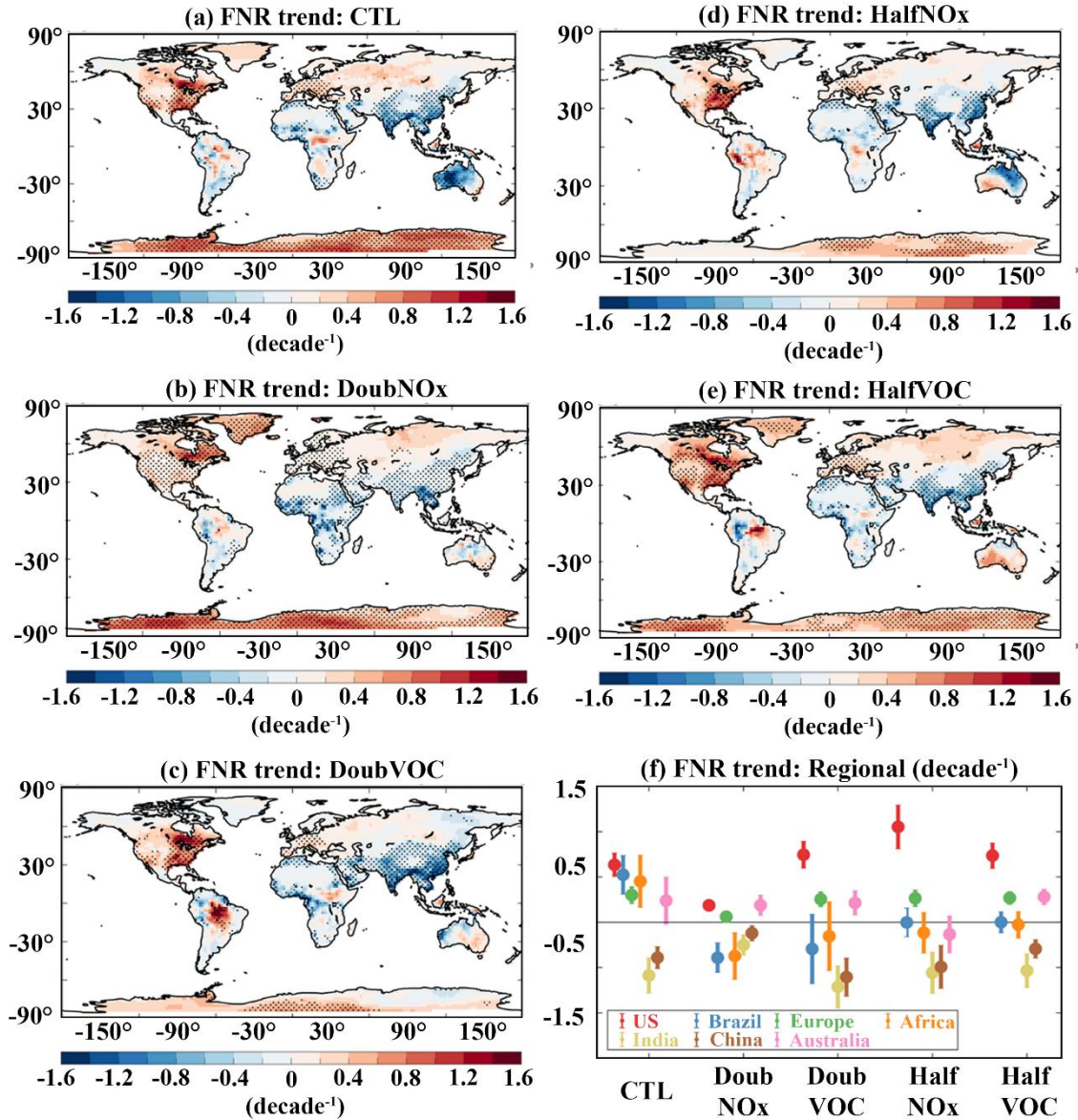
Figure 13. Trends in the tropospheric column HCHO/NO₂ ratio during 1998 – 2019 from ECHAM6–HAMMOZ simulations for (a) for CTL, (b) DoubNOx, (c) DoubVOC, (d) HalfNOx, (e) HalfVOC simulations. The stippled region indicates the trend significant at 95% confidence based on the t-test. (f) scatter plot illustrating the long-term trend and standard deviation over the regions depicted in Fig.9.

7. Tropospheric ozone radiative effects

The impact of emission changes on the tropospheric ozone radiative effect (TO3RE) is estimated using the ECHAM6 model output and a radiative kernel method (see data and model experiments). The estimated TO3RE for different model simulations are shown in Figure 14.

1043   In the CTL simulations (Fig. 14a), the estimated global mean area-weighted average TO3RE

1044   for the period 1998 to 2019 is 1.21 [1.1 to 1.3] W m^{-2}. High TO3RE is noted over North Africa

1045   and the Middle East region in NH (~2.2 W m^{-2}), while in SH, it is over Australia and South

1046   Africa (~1.2 W m^{-2}). TO3RE estimates from TES measurements (2005 – 2009) also show a

1047   peak of 1.0 W m^{-2} in northern Africa, the Mediterranean, and the Middle East in June–July–

1048   August (Bowman et al. 2013). Recently, Pope et al. (2024) reported TO3RE estimates from

1049   IASI–SOFID, IASI–FORLI, and IASI–IMS for the period 2008 – 2017. The values reported

1050   by Pope et al. (2024) are comparable with our CTL simulation (e.g. IASI–FORLI: 1.23 W m^{-2},

1051   IASI–SOFRID: 1.21 W m^{-2}, IASI–IMS: 1.21 W m^{-2}, ECHAM6: 1.22 W m^{-2}).

1052

1053   The anomalies of TO3RE from DoubNOx-CTL simulations are shown in Figure 14b. Doubling

1054   of NOx emission causes an enhancement in TO3RE by 0.36 [0.23 to 0.5] W m^{-2} compared to

1055   the CTL simulation. It shows a peak over the Middle East and adjacent North Africa (0.7 W

1056   m^{-2}). A similar peak over this region is also seen in the CTL simulation. Doubling of VOC

1057   emissions causes a marginal decrease in global mean TO3RE by -0.005 [-0.05 to 0.04] W m^{-2}.

1058   TRCO enhancement for doubling NOx is also higher than doubling VOC (see Fig.3).

1059   DoubVOC-CTL simulations (Fig. 14 c) show a peak over the Arctic (0.02 W m^{-2}). The TO3RE

1060   anomalies are negative between 30° N – 30° S. These negative anomalies in TO3RE between

1061   30° S – 30° N (Fig. 14c) can be attributed to negative anomalies of TRCO (Fig. 3h).

1062   The reduction of NOx emission by 50% reduced global mean TO3RE by -0.12 [-0.2 to -0.05]

1063   W m^{-2} than CTL. The anomalies in TO3RE from HalfNOx-CTL simulations (Fig. 14d) show

1064   negative anomalies all over the globe, with a strong decrease over the Middle East and adjacent

1065   North Africa (-0.25 W m^{-2}). Figures 14b and 14d show that the effect of

1066   enhancement/reduction of NOx emission is high over the Middle East and adjacent North

1067   Africa. The reduction of VOC emission by 50% reduced global mean TO3RE by -0.03 [-0.07

1068   to 0.02] W m^{-2} than CTL simulations (Fig. 14e). HalfVOC - CTL simulations show negative

1069   anomalies of TO3RE between 40° S – 40° N and positive 0.015 W m^{-2} (low confidence) over

1070   mid-high latitudes in NH and SH. From Figure 14, it is interesting to note that the magnitude

1071   of TO3RE and its response to emission change is pronounced over the Middle East compared

1072   to all other regions. Further, Figure 14f depicts the latitude variation of zonal mean TO3RE for

1073   different sensitivity simulations. It is clear from Figure 14f that the TO3RE response to

1074   emission change is large at the northern and southern mid-latitudes, around ±30°. Also, Figure

14f clearly indicates that the impacts of NOx emission changes are larger than VOCs throughout the latitude band.
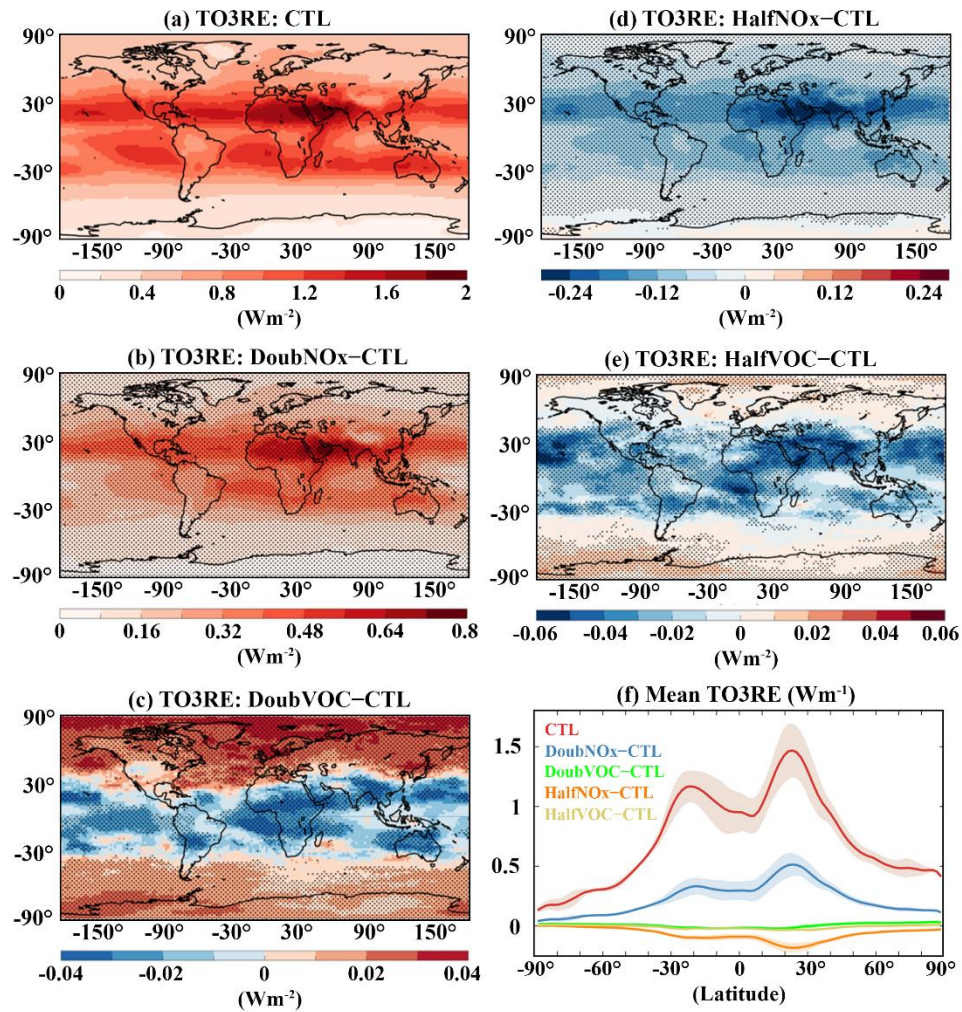
Figure 14. Tropospheric Ozone radiative effects (TO3RE) (W m^{-2}) for (a) CTL, and anomalies from (b) DoubNOx - CTL, (c) DoubVOC - CTL, (d) HalfNOx - CTL, (e) HalfVOC - CTL simulations. Stippled regions in Figures (b–e) indicate TO3RE significant at 95 % confidence level based on the t-test, (f) line plot for zonal mean TO3RE (W m^{-2}) from CTL, DoubNOx - CTL, DoubVOC - CTL, HalfNOx - CTL, HalfVOC - CTL, shades indicate standard deviation.

8 Summary and Conclusions

In this study, we report variation of tropospheric ozone levels, trends, photochemical regimes and radiative effects using the state-of-the-art ECHAM6–HAMMOZ chemistry-climate model simulations from 1998 to 2019. The model simulations are validated against multiple satellite observations. Our analysis shows that

1103   1. The estimated global mean trend in TRCO from CTL simulations for the period 1998 –
1104   2019 is 0.89 [-0.07 to 2.1] ppb decade^{-1}. Trend estimates from OMI/MLS (1.43 [-0.5 to
1105   3.2] ppb decade^{-1}) for the period January 2005 to December 2019 show good agreement
1106   with CTL (1.58 [0.3 to 3.3] ppb decade^{-1}) for the same period.

1107   2. TRCO anomalies from DoubNOx - CTL simulations show positive trends over Europe, the
1108   US, Africa, and South America, with a global mean trend of 1.2 [-0.1 to 2.7] ppb decade^{-1}.
1109   However, India and China show decreasing TRCO trend -2 to -4 ppb decade^{-1}. Surface
1110   ozone anomalies over these regions show strong negative trends -4.8 to -8 ppb decade^{-1}.

1111   3. Global mean TRCO trend anomalies from DOUBNOX - CTL simulation is 1.2 [-0.1 to
1112   2.7] ppb decade^{-1}, while for DoubVOC - CTL is 0.5 [-0.03 to 1.04] ppb decade^{-1}. Global
1113   mean TRCO trend anomalies from HalfNOx - CTL is 0.47 [-0.76 to 1.3] ppb decade^{-1} and
1114   for HalfVOC - CTL is 0.37 [-0.35 to 1.02] ppb decade^{-1}.

1115   4. The spatial distribution of TRCO anomalies shows that enhancement is nearly 12 times
1116   higher in DoubNOx - CTL than in DoubVOC - CTL simulations. The largest increase in
1117   surface ozone anomalies from DoubVOC - CTL is observed over Indo-Gangetic Plains,
1118   Eastern China and the eastern United States (4 – 6 ppb), where a decrease in surface ozone
1119   anomalies is observed in the DoubNOx - CTL simulation. This decrease (increase) in ozone
1120   with an increase in NOx (VOC) indicates that these regions are VOC-limited.

1121   5. The FNR shows that the transition from VOC–limited to NOx–limited happens suddenly
1122   in response to changes in the emission of NOx/VOC over the US and China. Whereas this
1123   transition region shows a wider range in Central Africa. Most polluted cities/industrialized
1124   areas in the US, Canada, Europe, west Russia, East China, Korea and Japan are identified
1125   with a low FNR, indicating VOC limited (FNRs <2). Meanwhile, NOx–limited regimes
1126   (largest FNR values >5) are primarily found in tropical rainforests, savannas, and arid
1127   climates.

1128   6. The DoubNOx simulation shows a notable change in the spatial extent of VOC–limited
1129   regimes, particularly in the NH. While the SH exhibits minimal change in the spatial extent
1130   of VOC–limited regimes.

1131   7. DoubVOC simulations reveal persistent VOC–limited regimes over Western Europe, with
1132   moderate FNR values indicating a transition to NOx–limited regimes across most of the
1133   NH. Comparing CTL and HalfNOx simulations globally shows a shift from VOC to NOx–
1134   limited regimes.

8. Comparison of all the emission simulations, DoubNOx and HalfNOx simulations influence the shift in tropospheric ozone photochemical regimes compared to DoubVOC and HalfVOC simulations, highlighting the global sensitivity of ozone photochemistry to NOx emissions changes.

9. Trends estimated from modelled FNR are negative over India (-0.6 decade^{-1}) and China (-0.4 decade^{-1}) in all the simulations, indicating that these regions have a tendency to become VOC–limited, while the positive trends over Europe (0.3 decade^{-1}), US (0.63 decade^{-1}), and Africa (0.45 decade^{-1}), indicating a tendency to become more NOx–limited.

10. The estimated global mean tropospheric ozone radiative effect (TO3RE) is 1.21 [1.1 to 1.3] W m^{-2} which is increased by the doubling of NO$_X$ emissions (DoubNOx - CTL) by 0.36 [0.23 to 0.5] W m^{-2} and VOCs by -0.005 [-0.05 to 0.04] W m^{-2} (DoubVOC - CTL). However, halving NOx (HalfNOx - CTL) emissions shows a reduction in the global mean TO3RE by -0.12 [-0.2 to -0.05] W m^{-2} and VOC (HalfVOC - CTL) by -0.03 [-0.07 to 0.02] W m^{-2}.

11. We show that anthropogenic NO$_X$ emissions have a higher impact on tropospheric ozone levels, trends, and radiative effects than VOC emissions globally.

Our study highlights the dominant role of anthropogenic NOx emissions in shaping tropospheric ozone trends, photochemical regimes, and radiative forcing over the past two decades. Sensitivity experiments reveal that NOx emission changes have a significantly larger impact on ozone levels and radiative forcing than VOCs, with regions transitioning from VOC-limited to NOx-limited regimes as NOx reductions continue. With current emission trends, air quality regulations, and industrial growth continuing to evolve, our study reinforces the need for region-specific mitigation strategies to effectively manage ozone pollution. This study emphasizes the importance of carefully balancing NOx and VOC controls to optimize air quality management and climate mitigation efforts. While climate change affects ozone chemistry, its impact over our study period (1998–2019) is minimal, given the relatively small global rate of temperature increase (~0.3–0.4°C) (IPCC AR6). Studies suggest that an ozone climate penalty emerges only after a 2–3°C temperature increase (Zanis et al., 2022), primarily in high-emission regions. Furthermore, rising temperatures increase water vapor, which reduces the ozone lifetime in remote areas. Thus, while climate change will play a growing role in future ozone variability, our findings confirm that anthropogenic emissions remain the dominant driver of recent ozone trends. As mitigation strategies evolve, targeted NOx and VOC controls must account for regional photochemical regimes, while future research should explore the potential interactions between climate change, natural VOCs, and ozone formation in a warming world.

1168 **Author's contribution**: SF and YE initiated the manuscript. SF made the model simulations.
1169 VS and SC did the analysis of model simulations. Satellite datasets are provided by JZ, BB,
1170 EF, IG, ID, MR, IS. All authors contributed to the writing of the manuscript.

1171

1172 **Competing interests:** At least one of the (co-)authors is a member of the editorial board of
1173 Atmospheric Chemistry and Physics.

1174

Acknowledgements

1176 S.F. acknowledge the high-performance computing at the Indian Institute of Tropical
1177 Meteorology Pune, India for supporting the model simulations. RJP was funded by the UK
1178 Natural Environment Research Council (NERC) by providing funding for the National Centre
1179 for Earth Observation (NCEO, award reference NE/R016518/1) and funding from the
1180 European Space Agency (ESA) Climate Change Initiative (CCI) post-doctoral fellowship
1181 scheme (award reference 4000137140).

Data availability

1183 Available from the TOAR FTP server (ftp://toar@ftpshare.al.noaa.gov).

Code availability

1185 Available from the corresponding author upon reasonable request.

References:

1187 Adame, J. A., Gutierrez-Alvarez, I., Cristofanelli, P., Notario, A., Bogeat, J. A., Bolivar, J. P.,
1188 and Yela, M.: Surface ozone trends at El Arenosillo observatory from a new perspective,
1189 Environmental Research, 214, 113887, https://doi.org/10.1016/j.envres.2022.113887, 2022.

1190 Alvarado, L. M. A., Richter, A., Vrekoussis, M., Hilboll, A., Kalisz Hedegaard, A. B.,
1191 Schneising, O., and Burrows, J. P.: Unexpected long-range transport of glyoxal and
1192 formaldehyde observed from the Copernicus Sentinel-5 Precursor satellite during the 2018
1193 Canadian wildfires, Atmos. Chem. Phys., 20, 2057-2072, 10.5194/acp-20-2057-2020, 2020.

1194 Anderson, D. C., Nicely, J. M., Wolfe, G. M., Hanisco, T. F., Salawitch, R. J., Canty, T. P.,
1195 Dickerson, R. R., Apel, E. C., Baidar, S., Bannan, T. J., Blake, N. J., Chen, D., Dix, B.,
1196 Fernandez, R. P., Hall, S. R., Hornbrook, R. S., Gregory Huey, L., Josse, B., Jöckel, P.,
1197 Kinnison, D. E., Koenig, T. K., Le Breton, M., Marécal, V., Morgenstern, O., Oman, L. D.,
1198 Pan, L. L., Percival, C., Plummer, D., Revell, L. E., Rozanov, E., Saiz-Lopez, A., Stenke, A.,
1199 Sudo, K., Tilmes, S., Ullmann, K., Volkamer, R., Weinheimer, A. J., and Zeng, G.:
1200 Formaldehyde in the Tropical Western Pacific: Chemical Sources and Sinks, Convective
1201 Transport, and Representation in CAM-Chem and the CCMI Models, Journal of Geophysical
1202 Research: Atmospheres, 122, 11, 201-211, 226, https://doi.org/10.1002/2016JD026121, 2017.

1203 Anglou, I., Glissenaar, I. A., Boersma, K. F., & Eskes, H. (2024). ESA CCI+ OMI L3 monthly
1204 mean NO2 columns [Data set]. Royal Netherlands Meteorological Institute (KNMI).
1205 https://doi.org/10.21944/cci-no2-omi-l3

1206 Archibald, A. T., Neu, J. L., Elshorbany, Y. F., Cooper, O. R., Young, P. J., Akiyoshi, H., Cox,
1207 R. A., Coyle, M., Derwent, R. G., Deushi, M., Finco, A., Frost, G. J., Galbally, I. E., Gerosa,
1208 G., Granier, C., Griffiths, P. T., Hossaini, R., Hu, L., Jöckel, P., Josse, B., Lin, M. Y., Mertens,
1209 M., Morgenstern, O., Naja, M., Naik, V., Oltmans, S., Plummer, D. A., Revell, L. E., Saiz-
1210 Lopez, A., Saxena, P., Shin, Y. M., Shahid, I., Shallcross, D., Tilmes, S., Trickl, T., Wallington,
1211 T. J., Wang, T., Worden, H. M., and Zeng, G.: Tropospheric Ozone Assessment Report: A
1212 critical review of changes in the tropospheric ozone burden and budget from 1850 to 2100,
1213 Elementa: Science of the Anthropocene, 8, 10.1525/elementa.2020.034, 2020.

1214 Barret, B., Gouzenes, Y., Le Flochmoen, E., and Ferrant, S.: Retrieval of Metop-A/IASI N2O
1215 Profiles and Validation with NDACC FTIR Data, Atmosphere, 12, 219, 2021.

1216 Barret, B., Le Flochmoen, E., Sauvage, B., Pavelin, E., Matricardi, M., and Cammas, J. P.: The
1217 detection of post-monsoon tropospheric ozone variability over south Asia using IASI data,
1218 Atmos. Chem. Phys., 11, 9533-9548, 10.5194/acp-11-9533-2011, 2011.

1219 Beig, G. and Singh, V.: Trends in tropical tropospheric column ozone from satellite data and
1220 MOZART model, Geophysical Research Letters, 34, https://doi.org/10.1029/2007GL030460,
1221 2007.

1222 Boersma, K. F., Vinken, G. C. M., and Eskes, H. J.: Representativeness errors in comparing
1223 chemistry transport and chemistry climate models with satellite UV–Vis tropospheric column
1224 retrievals, Geosci. Model Dev., 9, 875-898, 10.5194/gmd-9-875-2016, 2016.

1225 Borbas, E. and Ruston, B.: The RTTOV UWiremis IR land surface emissivity module, Mission
1226 Report EUMETSAT NWPSAF-MO-VS-042. http://nwpsaf.eu/vs_reports/nwpsaf-mo-vs-
1227 042.pdf, 2010.

1228 Chang, C.-Y., Faust, E., Hou, X., Lee, P., Kim, H. C., Hedquist, B. C., and Liao, K.-J.:
1229 Investigating ambient ozone formation regimes in neighboring cities of shale plays in the
1230 Northeast United States using photochemical modeling and satellite retrievals, Atmospheric
1231 Environment, 142, 152-170, https://doi.org/10.1016/j.atmosenv.2016.06.058, 2016.

1232 Chang, K.-L., Cooper, O. R., Gaudel, A., Allaart, M., Ancellet, G., Clark, H., Godin-
1233 Beekmann, S., Leblanc, T., Van Malderen, R., Nédélec, P., Petropavlovskikh, I., Steinbrecht,
1234 W., Stübi, R., Tarasick, D. W., and Torres, C.: Impact of the COVID-19 Economic Downturn
1235 on Tropospheric Ozone Trends: An Uncertainty Weighted Data Synthesis for Quantifying
1236 Regional Anomalies Above Western North America and Europe, AGU Advances, 3,
1237 e2021AV000542, https://doi.org/10.1029/2021AV000542, 2022.

1238 Chang, K.-L., Cooper, O. R., Rodriguez, G., Iraci, L. T., Yates, E. L., Johnson, M. S., Gaudel,
1239 A., Jaffe, D. A., Bernays, N., Clark, H., Effertz, P., Leblanc, T., Petropavlovskikh, I., Sauvage,
1240 B., and Tarasick, D. W.: Diverging Ozone Trends Above Western North America: Boundary
1241 Layer Decreases Versus Free Tropospheric Increases, Journal of Geophysical Research:
1242 Atmospheres, 128, e2022JD038090, https://doi.org/10.1029/2022JD038090, 2023.

1243 Chen, Y., Wang, M., Yao, Y., Zeng, C., Zhang, W., Yan, H., Gao, P., Fan, L., and Ye, D.:
1244 Research on the ozone formation sensitivity indicator of four urban agglomerations of China

1245 using Ozone Monitoring Instrument (OMI) satellite data and ground-based measurements,
1246 Science of The Total Environment, 869, 161679,
1247 https://doi.org/10.1016/j.scitotenv.2023.161679, 2023.

1248 Cohen, Y., Petetin, H., Thouret, V., Marécal, V., Josse, B., Clark, H., Sauvage, B., Fontaine,
1249 A., Athier, G., Blot, R., Boulanger, D., Cousin, J. M., and Nédélec, P.: Climatology and long-
1250 term evolution of ozone and carbon monoxide in the upper troposphere–lower stratosphere
1251 (UTLS) at northern midlatitudes, as seen by IAGOS from 1995 to 2013, Atmos. Chem. Phys.,
1252 18, 5415-5453, 10.5194/acp-18-5415-2018, 2018.

1253 Cooper, O. R., Parrish, D. D., Ziemke, J., Balashov, N. V., Cupeiro, M., Galbally, I. E., Gilge,
1254 S., Horowitz, L., Jensen, N. R., Lamarque, J.-F., Naik, V., Oltmans, S. J., Schwab, J., Shindell,
1255 D. T., Thompson, A. M., Thouret, V., Wang, Y., and Zbinden, R. M.: Global distribution and
1256 trends of tropospheric ozone: An observation-based review, Elementa: Science of the
1257 Anthropocene, 2, 10.12952/journal.elementa.000029, 2014.

1258 Cuesta, J., Kanaya, Y., Takigawa, M., Dufour, G., Eremenko, M., Foret, G., Miyazaki, K., and
1259 Beekmann, M.: Transboundary ozone pollution across East Asia: daily evolution and
1260 photochemical production analysed by IASI + GOME2 multispectral satellite observations and
1261 models, Atmos. Chem. Phys., 18, 9499-9525, 10.5194/acp-18-9499-2018, 2018.

1262 Cuesta, J., Costantino, L., Beekmann, M., Siour, G., Menut, L., Bessagnet, B., Landi, T. C.,
1263 Dufour, G., and Eremenko, M.: Ozone pollution during the COVID-19 lockdown in the spring
1264 of 2020 over Europe, analysed from satellite observations, in situ measurements, and models,
1265 Atmos. Chem. Phys., 22, 4471-4489, 10.5194/acp-22-4471-2022, 2022.

1266 Cuesta, J., Eremenko, M., Liu, X., Dufour, G., Cai, Z., Höpfner, M., von Clarmann, T., Sellitto,
1267 P., Foret, G., Gaubert, B., Beekmann, M., Orphal, J., Chance, K., Spurr, R., and Flaud, J. M.:
1268 Satellite observation of lowermost tropospheric ozone by multispectral synergism of IASI
1269 thermal infrared and GOME-2 ultraviolet measurements over Europe, Atmos. Chem. Phys.,
1270 13, 9675-9693, 10.5194/acp-13-9675-2013, 2013.

1271 De Smedt, I., Stavrakou, T., Hendrick, F., Danckaert, T., Vlemmix, T., Pinardi, G., Theys, N.,
1272 Lerot, C., Gielen, C., Vigouroux, C., Hermans, C., Fayt, C., Veefkind, P., Müller, J. F., and
1273 Van Roozendael, M.: Diurnal, seasonal and long-term variations of global formaldehyde
1274 columns inferred from combined OMI and GOME-2 observations, Atmos. Chem. Phys., 15,
1275 12519-12545, 10.5194/acp-15-12519-2015, 2015.

1276 De Smedt, I., Theys, N., Yu, H., Danckaert, T., Lerot, C., Compernolle, S., Van Roozendael,
1277 M., Richter, A., Hilboll, A., Peters, E., Pedergnana, M., Loyola, D., Beirle, S., Wagner, T.,
1278 Eskes, H., van Geffen, J., Boersma, K. F., and Veefkind, P.: Algorithm theoretical baseline for
1279 formaldehyde retrievals from S5P TROPOMI and from the QA4ECV project, Atmos. Meas.
1280 Tech., 11, 2395-2426, 10.5194/amt-11-2395-2018, 2018.

1281 De Smedt, I., Pinardi, G., Vigouroux, C., Compernolle, S., Bais, A., Benavent, N., Boersma,
1282 F., Chan, K. L., Donner, S., Eichmann, K. U., Hedelt, P., Hendrick, F., Irie, H., Kumar, V.,
1283 Lambert, J. C., Langerock, B., Lerot, C., Liu, C., Loyola, D., Piters, A., Richter, A., Rivera
1284 Cárdenas, C., Romahn, F., Ryan, R. G., Sinha, V., Theys, N., Vlietinck, J., Wagner, T., Wang,
1285 T., Yu, H., and Van Roozendael, M.: Comparative assessment of TROPOMI and OMI
1286 formaldehyde observations and validation against MAX-DOAS network column
1287 measurements, Atmos. Chem. Phys., 21, 12561-12593, 10.5194/acp-21-12561-2021, 2021.

Duncan, B. N., Yoshida, Y., Olson, J. R., Sillman, S., Martin, R. V., Lamsal, L., Hu, Y., Pickering, K. E., Retscher, C., Allen, D. J., and Crawford, J. H.: Application of OMI observations to a space-based indicator of NOx and VOC controls on surface ozone formation, Atmospheric Environment, 44, 2213-2223, https://doi.org/10.1016/j.atmosenv.2010.03.010, 2010.

Edwards, J. M. and Slingo, A.: Studies with a flexible new radiation code. I: Choosing a configuration for a large-scale model, Quarterly Journal of the Royal Meteorological Society, 122, 689-719, https://doi.org/10.1002/qj.49712253107, 1996.

Elshorbany, Y., Ziemke, J., Strode, S., Petetin, H., Miyazaki, K., De Smedt, I., Pickering, K., Seguel, R., Worden, H., Emmerichs, T., Taraborrelli, D., Cazorla, M., Fadnavis, S., Buchholz, R., Gaubert, B., Rojas, N., Nogueira, T., Salameh, T., and Huang, M.: Tropospheric Ozone Precursors: Global and Regional Distributions, Trends and Variability, EGUsphere, 2024, 1-57, 10.5194/egusphere-2024-720, 2024.

Emmons, L. K., Apel, E. C., Lamarque, J. F., Hess, P. G., Avery, M., Blake, D., Brune, W., Campos, T., Crawford, J., DeCarlo, P. F., Hall, S., Heikes, B., Holloway, J., Jimenez, J. L., Knapp, D. J., Kok, G., Mena-Carrasco, M., Olson, J., O'Sullivan, D., Sachse, G., Walega, J., Weibring, P., Weinheimer, A., and Wiedinmyer, C.: Impact of Mexico City emissions on regional air quality from MOZART-4 simulations, Atmos. Chem. Phys., 10, 6195-6212, 10.5194/acp-10-6195-2010, 2010.

EPA, O. U. Air Pollutant Emissions Trends Data. https://www.epa.gov/air-emissions-inventories/air-pollutant-emissions-trends-data, 2023

Fadnavis, S., Sabin, T. P., Rap, A., Müller, R., Kubin, A., and Heinold, B.: The impact of COVID-19 lockdown measures on the Indian summer monsoon, Environmental Research Letters, 16, 074054, 10.1088/1748-9326/ac109c, 2021a.

Fadnavis, S., Heinold, B., Sabin, T. P., Kubin, A., Huang, K., Rap, A., and Müller, R.: Air pollution reductions caused by the COVID-19 lockdown open up a way to preserve the Himalayan glaciers, Atmos. Chem. Phys., 23, 10439-10449, 10.5194/acp-23-10439-2023, 2023.

Fadnavis, S., Sabin, T. P., Roy, C., Rowlinson, M., Rap, A., Vernier, J.-P., and Sioris, C. E.: Elevated aerosol layer over South Asia worsens the Indian droughts, Scientific Reports, 9, 10268, 10.1038/s41598-019-46704-9, 2019a.

Fadnavis, S., Müller, R., Kalita, G., Rowlinson, M., Rap, A., Li, J. L. F., Gasparini, B., and Laakso, A.: The impact of recent changes in Asian anthropogenic emissions of SO2 on sulfate loading in the upper troposphere and lower stratosphere and the associated radiative changes, Atmos. Chem. Phys., 19, 9989-10008, 10.5194/acp-19-9989-2019, 2019b.

Fadnavis, S., Chavan, P., Joshi, A., Sonbawne, S. M., Acharya, A., Devara, P. C. S., Rap, A., Ploeger, F., and Müller, R.: Tropospheric warming over the northern Indian Ocean caused by South Asian anthropogenic aerosols: possible impact on the upper troposphere and lower stratosphere, Atmos. Chem. Phys., 22, 7179-7191, 10.5194/acp-22-7179-2022, 2022.

Fadnavis, S., Müller, R., Chakraborty, T., Sabin, T. P., Laakso, A., Rap, A., Griessbach, S., Vernier, J.-P., and Tilmes, S.: The role of tropical volcanic eruptions in exacerbating Indian droughts, Scientific Reports, 11, 2714, 10.1038/s41598-021-81566-0, 2021b.

Fiore, A. M., Hancock, S. E., Lamarque, J.-F., Correa, G. P., Chang, K.-L., Ru, M., Cooper, O., Gaudel, A., Polvani, L. M., Sauvage, B., and Ziemke, J. R.: Understanding recent tropospheric ozone trends in the context of large internal variability: a new perspective from chemistry-climate model ensembles, Environmental Research: Climate, 1, 025008, 10.1088/2752-5295/ac9cc2, 2022.

Fleming, Z. L., Doherty, R. M., von Schneidemesser, E., Malley, C. S., Cooper, O. R., Pinto, J. P., Colette, A., Xu, X., Simpson, D., Schultz, M. G., Lefohn, A. S., Hamad, S., Moolla, R., Solberg, S., and Feng, Z.: Tropospheric Ozone Assessment Report: Present-day ozone distribution and trends relevant to human health, Elementa: Science of the Anthropocene, 6, 10.1525/elementa.273, 2018.

Forster, P., Storelvmo, T., Armour, K., Collins, W., Dufresne, J.-L., Frame, D., Lunt, D. J., Mauritsen, T., Palmer, M. D., Watanabe, M., Wild, M., and Zhang, H.: The Earth's Energy Budget, Climate Feedbacks and Climate Sensitivity, in: Climate Change 2021: The Physical Science Basis. Contribution of Working Group I to the Sixth Assessment Report of the Intergovernmental Panel on Climate Change [Masson-Delmotte, V., P. Zhai, A. Pirani, S.L. Connors, C. Péan, S. Berger, N. Caud, Y. Chen, L. Goldfarb, M.I. Gomis, M. Huang, K. Leitzell, E. Lonnoy, J.B.R. Matthews, T.K. Maycock, T. Waterfield, O. Yelekçi, R. Yu, and B. Zhou (eds.)], edited by: Intergovernmental Panel on Climate, C., Cambridge University Press, Cambridge, 923-1054, DOI: 10.1017/9781009157896.009, 2021.

Forster, P. M., Smith, C., Walsh, T., Lamb, W. F., Lamboll, R., Hall, B., Hauser, M., Ribes, A., Rosen, D., Gillett, N. P., Palmer, M. D., Rogelj, J., von Schuckmann, K., Trewin, B., Allen, M., Andrew, R., Betts, R. A., Borger, A., Boyer, T., Broersma, J. A., Buontempo, C., Burgess, S., Cagnazzo, C., Cheng, L., Friedlingstein, P., Gettelman, A., Gütschow, J., Ishii, M., Jenkins, S., Lan, X., Morice, C., Mühle, J., Kadow, C., Kennedy, J., Killick, R. E., Krummel, P. B., Minx, J. C., Myhre, G., Naik, V., Peters, G. P., Pirani, A., Pongratz, J., Schleussner, C. F., Seneviratne, S. I., Szopa, S., Thorne, P., Kovilakam, M. V. M., Majamäki, E., Jalkanen, J. P., van Marle, M., Hoesly, R. M., Rohde, R., Schumacher, D., van der Werf, G., Vose, R., Zickfeld, K., Zhang, X., Masson-Delmotte, V., and Zhai, P.: Indicators of Global Climate Change 2023: annual update of key indicators of the state of the climate system and human influence, Earth Syst. Sci. Data, 16, 2625-2658, 10.5194/essd-16-2625-2024, 2024.

Gaudel, A., Bourgeois, I., Li, M., Chang, K. L., Ziemke, J., Sauvage, B., Stauffer, R. M., Thompson, A. M., Kollonige, D. E., Smith, N., Hubert, D., Keppens, A., Cuesta, J., Heue, K. P., Veefkind, P., Aikin, K., Peischl, J., Thompson, C. R., Ryerson, T. B., Frost, G. J., McDonald, B. C., and Cooper, O. R.: Tropical tropospheric ozone distribution and trends from in situ and satellite data, EGUsphere, 2024, 1-51, 10.5194/egusphere-2023-3095, 2024.

Gaudel, A., Cooper, O. R., Ancellet, G., Barret, B., Boynard, A., Burrows, J. P., Clerbaux, C., Coheur, P.-F., Cuesta, J., Cuevas, E., Doniki, S., Dufour, G., Ebojie, F., Foret, G., Garcia, O., Granados-Muñoz, M. J., Hannigan, J. W., Hase, F., Hassler, B., Huang, G., Hurtmans, D., Jaffe, D., Jones, N., Kalabokas, P., Kerridge, B., Kulawik, S., Latter, B., Leblanc, T., Le Flochmoën, E., Lin, W., Liu, J., Liu, X., Mahieu, E., McClure-Begley, A., Neu, J. L., Osman, M., Palm, M., Petetin, H., Petropavlovskikh, I., Querel, R., Rahpoe, N., Rozanov, A., Schultz, M. G., Schwab, J., Siddans, R., Smale, D., Steinbacher, M., Tanimoto, H., Tarasick, D. W., Thouret, V., Thompson, A. M., Trickl, T., Weatherhead, E., Wespes, C., Worden, H. M., Vigouroux, C., Xu, X., Zeng, G., and Ziemke, J.: Tropospheric Ozone Assessment Report: Present-day distribution and trends of tropospheric ozone relevant to climate and global

atmospheric chemistry model evaluation, Elementa: Science of the Anthropocene, 6, 10.1525/elementa.291, 2018.

Glissenaar, I. A., Anglou, I., Boersma, K. F., & Eskes. H, ESA CCI+ TROPOMI L3 monthly mean NO2 columns [Data set]. Royal Netherlands Meteorological Institute (KNMI). https://doi.org/10.21944/CCI-NO2-TROPOMI-L3, 2024

Goldberg, D. L., Anenberg, S. C., Kerr, G. H., Mohegh, A., Lu, Z., and Streets, D. G.: TROPOMI NO2 in the United States: A Detailed Look at the Annual Averages, Weekly Cycles, Effects of Temperature, and Correlation With Surface NO2 Concentrations, Earth's Future, 9, e2020EF001665, https://doi.org/10.1029/2020EF001665, 2021.

Griffiths, P. T., Murray, L. T., Zeng, G., Shin, Y. M., Abraham, N. L., Archibald, A. T., Deushi, M., Emmons, L. K., Galbally, I. E., Hassler, B., Horowitz, L. W., Keeble, J., Liu, J., Moeini, O., Naik, V., O'Connor, F. M., Oshima, N., Tarasick, D., Tilmes, S., Turnock, S. T., Wild, O., Young, P. J., and Zanis, P.: Tropospheric ozone in CMIP6 simulations, Atmos. Chem. Phys., 21, 4187-4218, 10.5194/acp-21-4187-2021, 2021.

Guan, J., Jin, B., Ding, Y., Wang, W., Li, G., and Ciren, P.: Global Surface HCHO Distribution Derived from Satellite Observations with Neural Networks Technique, Remote Sensing, 13, 4055, 2021.

Guenther, A. B., Jiang, X., Heald, C. L., Sakulyanontvittaya, T., Duhl, T., Emmons, L. K., and Wang, X.: The Model of Emissions of Gases and Aerosols from Nature version 2.1 (MEGAN2.1): an extended and updated framework for modeling biogenic emissions, Geosci. Model Dev., 5, 1471-1492, 10.5194/gmd-5-1471-2012, 2012.

Gulev, S. K., Thorne, P. W., Ahn, J., Dentener, F. J., Domingues, C. M., Gerland, S., Gong, D., Kaufman, D. S., Nnamchi, H. C., Quaas, J., Rivera, J. A., Sathyendranath, S., Smith, S. L., Trewin, B., von Schuckmann, K., and Vose, R. S.: Changing State of the Climate System, in: Climate Change 2021 – The Physical Science Basis: Working Group I Contribution to the Sixth Assessment Report of the Intergovernmental Panel on Climate Change [Masson-Delmotte, V., P. Zhai, A. Pirani, S.L. Connors, C. Péan, S. Berger, N. Caud, Y. Chen, L. Goldfarb, M.I. Gomis, M. Huang, K. Leitzell, E. Lonnoy, J.B.R. Matthews, T.K. Maycock, T. Waterfield, O. Yelekçi, R. Yu, and B. Zhou (eds.)], edited by: Intergovernmental Panel on Climate, C., Cambridge University Press, Cambridge, 287-422, DOI: 10.1017/9781009157896.004, 2021.

Henrot, A. J., Stanelle, T., Schröder, S., Siegenthaler, C., Taraborrelli, D., and Schultz, M. G.: Implementation of the MEGAN (v2.1) biogenic emission model in the ECHAM6-HAMMOZ chemistry climate model, Geosci. Model Dev., 10, 903-926, 10.5194/gmd-10-903-2017, 2017.

Hoffmann, L. and Spang, R.: An assessment of tropopause characteristics of the ERA5 and ERA-Interim meteorological reanalyses, Atmos. Chem. Phys., 22, 4019–4046, https://doi.org/10.5194/acp-22-4019-2022, 2022.

Jin, X. and Holloway, T.: Spatial and temporal variability of ozone sensitivity over China observed from the Ozone Monitoring Instrument, Journal of Geophysical Research: Atmospheres, 120, 7229-7246, https://doi.org/10.1002/2015JD023250, 2015.

Jin, X., Fiore, A., Boersma, K. F., Smedt, I. D., and Valin, L.: Inferring Changes in Summertime Surface Ozone–NOx–VOC Chemistry over U.S. Urban Areas from Two Decades

of Satellite and Ground-Based Observations, Environmental Science & Technology, 54, 6518-6529, 10.1021/acs.est.9b07785, 2020.

Jin, X., Fiore, A. M., Murray, L. T., Valin, L. C., Lamsal, L. N., Duncan, B., Folkert Boersma, K., De Smedt, I., Abad, G. G., Chance, K., and Tonnesen, G. S.: Evaluating a Space-Based Indicator of Surface Ozone-NO-VOC Sensitivity Over Midlatitude Source Regions and Application to Decadal Trends, Journal of Geophysical Research: Atmospheres, 122, 10,439-410,461, https://doi.org/10.1002/2017JD026720, 2017.

Johnson, M. S., Philip, S., Meech, S., Kumar, R., Sorek-Hamer, M., Shiga, Y. P., and Jung, J.: Insights into the long-term (2005–2021) spatiotemporal evolution of summer ozone production sensitivity in the Northern Hemisphere derived with the Ozone Monitoring Instrument (OMI), Atmos. Chem. Phys., 24, 10363-10384, 10.5194/acp-24-10363-2024, 2024.

Kinnison, D. E., Brasseur, G. P., Walters, S., Garcia, R. R., Marsh, D. R., Sassi, F., Harvey, V. L., Randall, C. E., Emmons, L., Lamarque, J. F., Hess, P., Orlando, J. J., Tie, X. X., Randel, W., Pan, L. L., Gettelman, A., Granier, C., Diehl, T., Niemeier, U., and Simmons, A. J.: Sensitivity of chemical tracers to meteorological parameters in the MOZART-3 chemical transport model, Journal of Geophysical Research: Atmospheres, 112, https://doi.org/10.1029/2006JD007879, 2007.

Kleinman, L. I.: Low and high NOx tropospheric photochemistry, Journal of Geophysical Research: Atmospheres, 99, 16831-16838, https://doi.org/10.1029/94JD01028, 1994.

Kumar, V., Beirle, S., Dörner, S., Mishra, A. K., Donner, S., Wang, Y., Sinha, V., and Wagner, T.: Long-term MAX-DOAS measurements of NO2, HCHO, and aerosols and evaluation of corresponding satellite data products over Mohali in the Indo-Gangetic Plain, Atmos. Chem. Phys., 20, 14183-14235, 10.5194/acp-20-14183-2020, 2020.

Lamarque, J. F., Emmons, L. K., Hess, P. G., Kinnison, D. E., Tilmes, S., Vitt, F., Heald, C. L., Holland, E. A., Lauritzen, P. H., Neu, J., Orlando, J. J., Rasch, P. J., and Tyndall, G. K.: CAM-chem: description and evaluation of interactive atmospheric chemistry in the Community Earth System Model, Geosci. Model Dev., 5, 369-411, 10.5194/gmd-5-369-2012, 2012.

Lamarque, J. F., Bond, T. C., Eyring, V., Granier, C., Heil, A., Klimont, Z., Lee, D., Liousse, C., Mieville, A., Owen, B., Schultz, M. G., Shindell, D., Smith, S. J., Stehfest, E., Van Aardenne, J., Cooper, O. R., Kainuma, M., Mahowald, N., McConnell, J. R., Naik, V., Riahi, K., and van Vuuren, D. P.: Historical (1850–2000) gridded anthropogenic and biomass burning emissions of reactive gases and aerosols: methodology and application, Atmos. Chem. Phys., 10, 7017-7039, 10.5194/acp-10-7017-2010, 2010.

Lamsal, L. N., Krotkov, N. A., Vasilkov, A., Marchenko, S., Qin, W., Yang, E. S., Fasnacht, Z., Joiner, J., Choi, S., Haffner, D., Swartz, W. H., Fisher, B., and Bucsela, E.: Ozone Monitoring Instrument (OMI) Aura nitrogen dioxide standard product version 4.0 with improved surface and cloud treatments, Atmos. Meas. Tech., 14, 455-479, 10.5194/amt-14-455-2021, 2021.

Lee, H.-J., Chang, L.-S., Jaffe, D. A., Bak, J., Liu, X., Abad, G. G., Jo, H.-Y., Jo, Y.-J., Lee, J.-B., Yang, G.-H., Kim, J.-M., and Kim, C.-H.: Satellite-Based Diagnosis and Numerical Verification of Ozone Formation Regimes over Nine Megacities in East Asia, Remote Sensing, 14, 1285, 2022.

1459 Lefohn, A. S., Malley, C. S., Simon, H., Wells, B., Xu, X., Zhang, L., and Wang, T.: Responses
1460 of human health and vegetation exposure metrics to changes in ozone concentration
1461 distributions in the European Union, United States, and China, Atmospheric Environment, 152,
1462 123-145, https://doi.org/10.1016/j.atmosenv.2016.12.025, 2017.

1463 Li, M., Kurokawa, J., Zhang, Q., Woo, J. H., Morikawa, T., Chatani, S., Lu, Z., Song, Y., Geng,
1464 G., Hu, H., Kim, J., Cooper, O. R., and McDonald, B. C.: MIXv2: a long-term mosaic emission
1465 inventory for Asia (2010–2017), Atmos. Chem. Phys., 24, 3925-3952, 10.5194/acp-24-3925-
1466 2024, 2024.

1467 Li, S., Yang, Y., Wang, H., Li, P., Li, K., Ren, L., Wang, P., Li, B., Mao, Y., and Liao, H.:
1468 Rapid increase in tropospheric ozone over Southeast Asia attributed to changes in precursor
1469 emission source regions and sectors, Atmospheric Environment, 304, 119776,
1470 https://doi.org/10.1016/j.atmosenv.2023.119776, 2023.

1471 Lin, M., Horowitz, L. W., Oltmans, S. J., Fiore, A. M., and Fan, S.: Tropospheric ozone trends
1472 at Mauna Loa Observatory tied to decadal climate variability, Nature Geoscience, 7, 136-143,
1473 10.1038/ngeo2066, 2014.

1474 Liu, J., Strode, S. A., Liang, Q., Oman, L. D., Colarco, P. R., Fleming, E. L., Manyin, M. E.,
1475 Douglass, A. R., Ziemke, J. R., Lamsal, L. N., and Li, C.: Change in Tropospheric Ozone in
1476 the Recent Decades and Its Contribution to Global Total Ozone, Journal of Geophysical
1477 Research: Atmospheres, 127, e2022JD037170, https://doi.org/10.1029/2022JD037170, 2022.

1478 Lu, X., Zhang, L., Liu, X., Gao, M., Zhao, Y., and Shao, J.: Lower tropospheric ozone over
1479 India and its linkage to the South Asian monsoon, Atmos. Chem. Phys., 18, 3101-3118,
1480 10.5194/acp-18-3101-2018, 2018.

1481 Mahajan, A. S., De Smedt, I., Biswas, M. S., Ghude, S., Fadnavis, S., Roy, C., and van
1482 Roozendael, M.: Inter-annual variations in satellite observations of nitrogen dioxide and
1483 formaldehyde over India, Atmospheric Environment, 116, 194-201,
1484 https://doi.org/10.1016/j.atmosenv.2015.06.004, 2015.

1485 Martin, R. V., Fiore, A. M., and Van Donkelaar, A.: Space-based diagnosis of surface ozone
1486 sensitivity to anthropogenic emissions, Geophysical Research Letters, 31,
1487 https://doi.org/10.1029/2004GL019416, 2004.

1488 Matricardi, M., Chevallier, F., Kelly, G., and Thépaut, J.-N.: An improved general fast radiative
1489 transfer model for the assimilation of radiance observations, Quarterly Journal of the Royal
1490 Meteorological Society, 130, 153-173, https://doi.org/10.1256/qj.02.181, 2004.

1491 Millet, D. B., Jacob, D. J., Boersma, K. F., Fu, T.-M., Kurosu, T. P., Chance, K., Heald, C. L.,
1492 and Guenther, A.: Spatial distribution of isoprene emissions from North America derived from
1493 formaldehyde column measurements by the OMI satellite sensor, Journal of Geophysical
1494 Research: Atmospheres, 113, https://doi.org/10.1029/2007JD008950, 2008.

1495 Mills, G., Pleijel, H., Malley, C. S., Sinha, B., Cooper, O. R., Schultz, M. G., Neufeld, H. S.,
1496 Simpson, D., Sharps, K., Feng, Z., Gerosa, G., Harmens, H., Kobayashi, K., Saxena, P.,
1497 Paoletti, E., Sinha, V., and Xu, X.: Tropospheric Ozone Assessment Report: Present-day
1498 tropospheric ozone distribution and trends relevant to vegetation, Elementa: Science of the
1499 Anthropocene, 6, 10.1525/elementa.302, 2018.

Monks, P. S., Archibald, A. T., Colette, A., Cooper, O., Coyle, M., Derwent, R., Fowler, D., Granier, C., Law, K. S., Mills, G. E., Stevenson, D. S., Tarasova, O., Thouret, V., von Schneidemesser, E., Sommariva, R., Wild, O., and Williams, M. L.: Tropospheric ozone and its precursors from the urban to the global scale from air quality to short-lived climate forcer, Atmos. Chem. Phys., 15, 8889-8973, 10.5194/acp-15-8889-2015, 2015.

Myhre, G., Shindell, D., Bréon, F. M., Collins, W., Fuglestvedt, J., Huang, J., Koch, D., Lamarque, J. F., Lee, D., Mendoza, B., Nakajima, T., Robock, A., Stephens, G., Takemura, T., and Zhang, H.: Anthropogenic and Natural Radiative Forcing, in: Climate Change 2013: The Physical Science Basis. Contribution of Working Group I to the Fifth Assessment Report of the Intergovernmental Panel on Climate Change [Stocker, T.F., D. Qin, G.-K. Plattner, M. Tignor, S.K. Allen, J. Boschung, A. Nauels, Y. Xia, V. Bex and P.M. Midgley (eds.)], edited by: Intergovernmental Panel on Climate, C., Cambridge University Press, Cambridge, 659-740, doi:10.1017/CBO9781107415324.020, 2013.

O3 (IASI+GOME2) – IASI portal: https://iasi.aeris-data.fr/o3_iago2/, last access: 28 May 2024

Okamoto, S., Cuesta, J., Beekmann, M., Dufour, G., Eremenko, M., Miyazaki, K., Boonne, C., Tanimoto, H., and Akimoto, H.: Impact of different sources of precursors on an ozone pollution outbreak over Europe analysed with IASI+GOME2 multispectral satellite observations and model simulations, Atmos. Chem. Phys., 23, 7399-7423, 10.5194/acp-23-7399-2023, 2023.

Pope, R. J., Rap, A., Pimlott, M. A., Barret, B., Le Flochmoen, E., Kerridge, B. J., Siddans, R., Latter, B. G., Ventress, L. J., Boynard, A., Retscher, C., Feng, W., Rigby, R., Dhomse, S. S., Wespes, C., and Chipperfield, M. P.: Quantifying the tropospheric ozone radiative effect and its temporal evolution in the satellite era, Atmos. Chem. Phys., 24, 3613-3626, 10.5194/acp-24-3613-2024, 2024.

Prather, M., and Zhu X., Lifetimes and timescales of tropospheric ozone, Lifetimes and timescales of tropospheric ozone. Elem, 12, 1, 2024, doi:10.1525/elementa.2023.00112.

Putero, D., Cristofanelli, P., Chang, K. L., Dufour, G., Beachley, G., Couret, C., Effertz, P., Jaffe, D. A., Kubistin, D., Lynch, J., Petropavlovskikh, I., Puchalski, M., Sharac, T., Sive, B. C., Steinbacher, M., Torres, C., and Cooper, O. R.: Fingerprints of the COVID-19 economic downturn and recovery on ozone anomalies at high-elevation sites in North America and western Europe, Atmos. Chem. Phys., 23, 15693-15709, 10.5194/acp-23-15693-2023, 2023.

Rap, A., Richards, N. A. D., Forster, P. M., Monks, S. A., Arnold, S. R., and Chipperfield, M. P.: Satellite constraint on the tropospheric ozone radiative effect, Geophysical Research Letters, 42, 5074-5081, https://doi.org/10.1002/2015GL064037, 2015.

Rast, S., Schultz, M. G., Bey, I., van Noije, T., Aghedo, A. M., Brasseur, G. P., Diehl, T., Esch, M., Ganzeveld, L., Kirchner, I., Kornblueh, L., Rhodin, A., Roeckner, E., Schmidt, H., Schroder, S., Schulzweida, U., Stier, P., Thomas, K., and Walters, S.: Evaluation of the tropospheric chemistry general circulation model ECHAM5–MOZ and its application to the analysis of the chemical composition of the troposphere with an emphasis on the late RETRO period 1990–2000, Max-Planck-Institut für Meteorologie, Hamburg114, 2014.

Reick, C. H., Raddatz, T., Brovkin, V., and Gayler, V.: Representation of natural and anthropogenic land cover change in MPI-ESM, Journal of Advances in Modeling Earth Systems, 5, 459-482, https://doi.org/10.1002/jame.20022, 2013.

Ren, J., Guo, F., and Xie, S.: Diagnosing ozone–NOx–VOC sensitivity and revealing causes of ozone increases in China based on 2013–2021 satellite retrievals, Atmos. Chem. Phys., 22, 15035-15047, 10.5194/acp-22-15035-2022, 2022.

Riese, M. and Ploeger, F. and Rap, A. and Vogel, B. and Konopka, P. and Dameris, M. and Forster, P.: Impact of uncertainties in atmospheric mixing on simulated UTLS composition and related radiative effects, J. Geophys. Res., 117, D16305, 10.1029/2012JD017751, 2012

Roberts, S. J., Salawitch, R. J., Wolfe, G. M., Marvin, M. R., Canty, T. P., Allen, D. J., Hall-Quinlan, D. L., Krask, D. J., and Dickerson, R. R.: Multidecadal trends in ozone chemistry in the Baltimore-Washington Region, Atmospheric Environment, 285, 119239, https://doi.org/10.1016/j.atmosenv.2022.119239, 2022.

Rosanka, S., Franco, B., Clarisse, L., Coheur, P. F., Pozzer, A., Wahner, A., and Taraborrelli, D.: The impact of organic pollutants from Indonesian peatland fires on the tropospheric and lower stratospheric composition, Atmos. Chem. Phys., 21, 11257-11288, 10.5194/acp-21-11257-2021, 2021.

Rothman, L. S., Jacquemart, D., Barbe, A., Chris Benner, D., Birk, M., Brown, L. R., Carleer, M. R., Chackerian, C., Chance, K., Coudert, L. H., Dana, V., Devi, V. M., Flaud, J. M., Gamache, R. R., Goldman, A., Hartmann, J. M., Jucks, K. W., Maki, A. G., Mandin, J. Y., Massie, S. T., Orphal, J., Perrin, A., Rinsland, C. P., Smith, M. A. H., Tennyson, J., Tolchenov, R. N., Toth, R. A., Vander Auwera, J., Varanasi, P., and Wagner, G.: The HITRAN 2004 molecular spectroscopic database, Journal of Quantitative Spectroscopy and Radiative Transfer, 96, 139-204, https://doi.org/10.1016/j.jqsrt.2004.10.008, 2005.

Rowlinson, M. J., Rap, A., Hamilton, D. S., Pope, R. J., Hantson, S., Arnold, S. R., Kaplan, J. O., Arneth, A., Chipperfield, M. P., Forster, P. M., and Nieradzik, L.: Tropospheric ozone radiative forcing uncertainty due to pre-industrial fire and biogenic emissions, Atmos. Chem. Phys., 20, 10937-10951, 10.5194/acp-20-10937-2020, 2020.

Saunders, R., Matricardi, M., and Brunel, P.: An improved fast radiative transfer model for assimilation of satellite radiance observations, Quarterly Journal of the Royal Meteorological Society, 125, 1407-1425, https://doi.org/10.1002/qj.1999.49712555615, 1999.

Schroeder, J. R., Crawford, J. H., Fried, A., Walega, J., Weinheimer, A., Wisthaler, A., Müller, M., Mikoviny, T., Chen, G., Shook, M., Blake, D. R., and Tonnesen, G. S.: New insights into the column CH2O/NO2 ratio as an indicator of near-surface ozone sensitivity, Journal of Geophysical Research: Atmospheres, 122, 8885-8907, https://doi.org/10.1002/2017JD026781, 2017.

Schultz, M. G., Stadtler, S., Schröder, S., Taraborrelli, D., Franco, B., Krefting, J., Henrot, A., Ferrachat, S., Lohmann, U., Neubauer, D., Siegenthaler-Le Drian, C., Wahl, S., Kokkola, H., Kühn, T., Rast, S., Schmidt, H., Stier, P., Kinnison, D., Tyndall, G. S., Orlando, J. J., and Wespes, C.: The chemistry–climate model ECHAM6.3-HAM2.3-MOZ1.0, Geosci. Model Dev., 11, 1695-1723, 10.5194/gmd-11-1695-2018, 2018.

Schultz, M. G., Schröder, S., Lyapina, O., Cooper, O. R., Galbally, I., Petropavlovskikh, I., von Schneidemesser, E., Tanimoto, H., Elshorbany, Y., Naja, M., Seguel, R. J., Dauert, U., Eckhardt, P., Feigenspan, S., Fiebig, M., Hjellbrekke, A.-G., Hong, Y.-D., Kjeld, P. C., Koide, H., Lear, G., Tarasick, D., Ueno, M., Wallasch, M., Baumgardner, D., Chuang, M.-T., Gillett, R., Lee, M., Molloy, S., Moolla, R., Wang, T., Sharps, K., Adame, J. A., Ancellet, G., Apadula,

F., Artaxo, P., Barlasina, M. E., Bogucka, M., Bonasoni, P., Chang, L., Colomb, A., Cuevas-Agulló, E., Cupeiro, M., Degorska, A., Ding, A., Fröhlich, M., Frolova, M., Gadhavi, H., Gheusi, F., Gilge, S., Gonzalez, M. Y., Gros, V., Hamad, S. H., Helmig, D., Henriques, D., Hermansen, O., Holla, R., Hueber, J., Im, U., Jaffe, D. A., Komala, N., Kubistin, D., Lam, K.-S., Laurila, T., Lee, H., Levy, I., Mazzoleni, C., Mazzoleni, L. R., McClure-Begley, A., Mohamad, M., Murovec, M., Navarro-Comas, M., Nicodim, F., Parrish, D., Read, K. A., Reid, N., Ries, L., Saxena, P., Schwab, J. J., Scorgie, Y., Senik, I., Simmonds, P., Sinha, V., Skorokhod, A. I., Spain, G., Spangl, W., Spoor, R., Springston, S. R., Steer, K., Steinbacher, M., Suharguniyawan, E., Torre, P., Trickl, T., Weili, L., Weller, R., Xiaobin, X., Xue, L., and Zhiqiang, M.: Tropospheric Ozone Assessment Report: Database and metrics data of global surface ozone observations, Elementa: Science of the Anthropocene, 5, 10.1525/elementa.244, 2017.

Scott, C. E., Monks, S. A., Spracklen, D. V., Arnold, S. R., Forster, P. M., Rap, A., Äijälä, M., Artaxo, P., Carslaw, K. S., Chipperfield, M. P., Ehn, M., Gilardoni, S., Heikkinen, L., Kulmala, M., Petäjä, T., Reddington, C. L. S., Rizzo, L. V., Swietlicki, E., Vignati, E., and Wilson, C.: Impact on short-lived climate forcers increases projected warming due to deforestation, Nature Communications, 9, 157, 10.1038/s41467-017-02412-4, 2018.

Shen, L., Jacob, D. J., Zhu, L., Zhang, Q., Zheng, B., Sulprizio, M. P., Li, K., De Smedt, I., González Abad, G., Cao, H., Fu, T.-M., and Liao, H.: The 2005–2016 Trends of Formaldehyde Columns Over China Observed by Satellites: Increasing Anthropogenic Emissions of Volatile Organic Compounds and Decreasing Agricultural Fire Emissions, Geophysical Research Letters, 46, 4468-4475, https://doi.org/10.1029/2019GL082172, 2019.

Sillman, S.: The use of NO , H2O2, and HNO3 as indicators for ozone-NO -hydrocarbon sensitivity in urban locations, Journal of Geophysical Research: Atmospheres, 100, 14175-14188, https://doi.org/10.1029/94JD02953, 1995.

Sillman, S., Logan, J. A., and Wofsy, S. C.: The sensitivity of ozone to nitrogen oxides and hydrocarbons in regional ozone episodes, Journal of Geophysical Research: Atmospheres, 95, 1837-1851, https://doi.org/10.1029/JD095iD02p01837, 1990.

Skeie, R. B., Myhre, G., Hodnebrog, Ø., Cameron-Smith, P. J., Deushi, M., Hegglin, M. I., Horowitz, L. W., Kramer, R. J., Michou, M., Mills, M. J., Olivié, D. J. L., Connor, F. M. O., Paynter, D., Samset, B. H., Sellar, A., Shindell, D., Takemura, T., Tilmes, S., and Wu, T.: Historical total ozone radiative forcing derived from CMIP6 simulations, npj Climate and Atmospheric Science, 3, 32, 10.1038/s41612-020-00131-0, 2020.

Sofieva, V. F., Tamminen, J., Kyrölä, E., Mielonen, T., Veefkind, P., Hassler, B., and Bodeker, G. E.: A novel tropopause-related climatology of ozone profiles, Atmos. Chem. Phys., 14, 283-299, 10.5194/acp-14-283-2014, 2014.

Souri, A. H., Choi, Y., Jeon, W., Woo, J.-H., Zhang, Q., and Kurokawa, J.-i.: Remote sensing evidence of decadal changes in major tropospheric ozone precursors over East Asia, Journal of Geophysical Research - Atmospheres, 122, 2474-2492, https://doi.org/10.1002/2016JD025663, 2017.

Stadtler, S., Simpson, D., Schröder, S., Taraborrelli, D., Bott, A., and Schultz, M.: Ozone impacts of gas–aerosol uptake in global chemistry transport models, Atmos. Chem. Phys., 18, 3147-3171, 10.5194/acp-18-3147-2018, 2018.

Steinbrecht, W., Kubistin, D., Plass-Dülmer, C., Davies, J., Tarasick, D. W., von der Gathen, P., Deckelmann, H., Jepsen, N., Kivi, R., Lyall, N., Palm, M., Notholt, J., Kois, B., Oelsner, P., Allaart, M., Piters, A., Gill, M., Van Malderen, R., Delcloo, A. W., Sussmann, R., Mahieu, E., Servais, C., Romanens, G., Stübi, R., Ancellet, G., Godin-Beekmann, S., Yamanouchi, S., Strong, K., Johnson, B., Cullis, P., Petropavlovskikh, I., Hannigan, J. W., Hernandez, J.-L., Diaz Rodriguez, A., Nakano, T., Chouza, F., Leblanc, T., Torres, C., Garcia, O., Röhling, A. N., Schneider, M., Blumenstock, T., Tully, M., Paton-Walsh, C., Jones, N., Querel, R., Strahan, S., Stauffer, R. M., Thompson, A. M., Inness, A., Engelen, R., Chang, K.-L., and Cooper, O. R.: COVID-19 Crisis Reduces Free Tropospheric Ozone Across the Northern Hemisphere, Geophysical Research Letters, 48, e2020GL091987, https://doi.org/10.1029/2020GL091987, 2021.

Stevens, B., Giorgetta, M., Esch, M., Mauritsen, T., Crueger, T., Rast, S., Salzmann, M., Schmidt, H., Bader, J., Block, K., Brokopf, R., Fast, I., Kinne, S., Kornblueh, L., Lohmann, U., Pincus, R., Reichler, T., and Roeckner, E.: Atmospheric component of the MPI-M Earth System Model: ECHAM6, Journal of Advances in Modeling Earth Systems , 5, 146-172, 10.1002/jame.20015, 2013.

Stevenson, D. S., Dentener, F. J., Schultz, M. G., Ellingsen, K., van Noije, T. P. C., Wild, O., Zeng, G., Amann, M., Atherton, C. S., Bell, N., Bergmann, D. J., Bey, I., Butler, T., Cofala, J., Collins, W. J., Derwent, R. G., Doherty, R. M., Drevet, J., Eskes, H. J., Fiore, A. M., Gauss, M., Hauglustaine, D. A., Horowitz, L. W., Isaksen, I. S. A., Krol, M. C., Lamarque, J. F., Lawrence, M. G., Montanaro, V., Müller, J. F., Pitari, G., Prather, M. J., Pyle, J. A., Rast, S., Rodriguez, J. M., Sanderson, M. G., Savage, N. H., Shindell, D. T., Strahan, S. E., Sudo, K., and Szopa, S.: Multimodel ensemble simulations of present-day and near-future tropospheric ozone, Journal of Geophysical Research-Atmospheres, 111, 10.1029/2005JD006338, 2006.

Surl, L., Palmer, P. I., and González Abad, G.: Which processes drive observed variations of HCHO columns over India?, Atmos. Chem. Phys., 18, 4549-4566, 10.5194/acp-18-4549-2018, 2018.

Szopa, S., Naik, V., Adhikary, B., Artaxo, P., Berntsen, T., Collins, W. D., Fuzzi, S., Gallardo, L., Kiendler-Scharr, A., Klimont, Z., Liao, H., Unger, N., and Zanis, P.: Short-lived Climate Forcers, in: Climate Change 2021: The Physical Science Basis. Contribution of Working Group I to the Sixth Assessment Report of the Intergovernmental Panel on Climate Change [Masson-Delmotte, V., P. Zhai, A. Pirani, S.L. Connors, C. Péan, S. Berger, N. Caud, Y. Chen, L. Goldfarb, M.I. Gomis, M. Huang, K. Leitzell, E. Lonnoy, J.B.R. Matthews, T.K. Maycock, T. Waterfield, O. Yelekçi, R. Yu, and B. Zhou (eds.)], edited by: Intergovernmental Panel on Climate, C., Cambridge University Press, Cambridge, 817-922, DOI: 10.1017/9781009157896.008, 2021.

Taraborrelli, D., Cabrera-Perez, D., Bacer, S., Gromov, S., Lelieveld, J., Sander, R., and Pozzer, A.: Influence of aromatics on tropospheric gas-phase composition, Atmos. Chem. Phys., 21, 2615-2636, 10.5194/acp-21-2615-2021, 2021.

Tarasick, D. W., Carey-Smith, T. K., Hocking, W. K., Moeini, O., He, H., Liu, J., Osman, M. K., Thompson, A. M., Johnson, B. J., Oltmans, S. J., and Merrill, J. T.: Quantifying stratosphere-troposphere transport of ozone using balloon-borne ozonesondes, radar windprofilers and trajectory models, Atmospheric Environment, 198, 496-509, https://doi.org/10.1016/j.atmosenv.2018.10.040, 2019.

Van Vuuren, D. P., Edmonds, J., Kainuma, M., Riahi, K., Thomson, A., Hibbard, K., Hurtt, G. C., Kram, T., Krey, V., Lamarque, J.-F., Masui, T., Meinshausen, M., Nakicenovic, N., Smith, S. J., and Rose, S. K.: The representative concentration pathways: an overview, Climatic Change, 109, 5, 10.1007/s10584-011-0148-z, 2011.

Veefkind, J. P., Aben, I., McMullan, K., Förster, H., de Vries, J., Otter, G., Claas, J., Eskes, H. J., de Haan, J. F., Kleipool, Q., van Weele, M., Hasekamp, O., Hoogeveen, R., Landgraf, J., Snel, R., Tol, P., Ingmann, P., Voors, R., Kruizinga, B., Vink, R., Visser, H., and Levelt, P. F.: TROPOMI on the ESA Sentinel-5 Precursor: A GMES mission for global observations of the atmospheric composition for climate, air quality and ozone layer applications, Remote Sensing of Environment, 120, 70-83, https://doi.org/10.1016/j.rse.2011.09.027, 2012.

Verstraeten, W. W., Neu, J. L., Williams, J. E., Bowman, K. W., Worden, J. R., and Boersma, K. F.: Rapid increases in tropospheric ozone production and export from China, Nature Geoscience, 8, 690-695, 10.1038/ngeo2493, 2015.

Vignati, E., Wilson, J., and Stier, P.: M7: An efficient size-resolved aerosol microphysics module for large-scale aerosol transport models, Journal of Geophysical Reseach, Atmospheres, 109, 10.1029/2003JD004485, 2004.

Wang, Y., Zhao, Y., Liu, Y. *et al.* Sustained emission reductions have restrained the ozone pollution over China. *Nat. Geosci.* **16**, 967–974 (2023). https://doi.org/10.1038/s41561-023-01284-2

Wang, H., Lu, X., Jacob, D. J., Cooper, O. R., Chang, K. L., Li, K., Gao, M., Liu, Y., Sheng, B., Wu, K., Wu, T., Zhang, J., Sauvage, B., Nédélec, P., Blot, R., and Fan, S.: Global tropospheric ozone trends, attributions, and radiative impacts in 1995–2017: an integrated analysis using aircraft (IAGOS) observations, ozonesonde, and multi-decadal chemical model simulations, Atmos. Chem. Phys., 22, 13753-13782, 10.5194/acp-22-13753-2022, 2022.

Wang, W., van der A, R., Ding, J., van Weele, M., and Cheng, T.: Spatial and temporal changes of the ozone sensitivity in China based on satellite and ground-based observations, Atmos. Chem. Phys., 21, 7253-7269, 10.5194/acp-21-7253-2021, 2021.

Wang, Y., Lampel, J., Xie, P., Beirle, S., Li, A., Wu, D., and Wagner, T.: Ground-based MAX-DOAS observations of tropospheric aerosols, NO2, SO2 and HCHO in Wuxi, China, from 2011 to 2014, Atmos. Chem. Phys., 17, 2189-2215, 10.5194/acp-17-2189-2017, 2017.

WMO, Meteorology – A three-dimensional science, World Meteorological Organisation, Bulletin 6, (Oct), 134–138, 1957.

Young, P. J., Naik, V., Fiore, A. M., Gaudel, A., Guo, J., Lin, M. Y., Neu, J. L., Parrish, D. D., Rieder, H. E., Schnell, J. L., Tilmes, S., Wild, O., Zhang, L., Ziemke, J., Brandt, J., Delcloo, A., Doherty, R. M., Geels, C., Hegglin, M. I., Hu, L., Im, U., Kumar, R., Luhar, A., Murray, L., Plummer, D., Rodriguez, J., Saiz-Lopez, A., Schultz, M. G., Woodhouse, M. T., and Zeng, G.: Tropospheric Ozone Assessment Report: Assessment of global-scale model performance for global and regional ozone distributions, variability, and trends, Elementa: Science of the Anthropocene, 6, 10.1525/elementa.265, 2018.

Zanis, P., Akritidis, D., Turnock, S., Naik, V., Szopa, S., Georgoulias, A.K., Bauer, S.E., Deushi, M., Horowitz, L.W., Keeble, J. and Le Sager, P., 2022. Climate change penalty and

benefit on surface ozone: a global perspective based on CMIP6 earth system models. Environmental Research Letters, 17(2), p.024014.

Zhang, Y. Q., Cooper, O. R., Gaudel, A., Thompson, A. M., Nédélec, P., Ogino, S. Y., and West, J. J.: Tropospheric ozone change from 1980 to 2010 dominated by equatorward redistribution of emissions, Nature Geoscience, 9, 875-+, 10.1038/NGEO2827, 2016.

Zhang, Y., West, J. J., Emmons, L. K., Flemming, J., Jonson, J. E., Lund, M. T., et al. (2021). Contributions of World Regions to the Global Tropospheric Ozone Burden Change from 1980 to 2010. *Geophysical Research Letters*, 48, e2020GL089184. https://doi.org/10.1029/2020GL089184

Ziemke, J. R., Chandra, S., and Bhartia, P. K.: A 25-year data record of atmospheric ozone in the Pacific from Total Ozone Mapping Spectrometer (TOMS) cloud slicing: Implications for ozone trends in the stratosphere and troposphere, Journal of Geophysical Research - Atmopsheres, 110, 10.1029/2004JD005687, 2005.

Ziemke, J. R., Chandra, S., Duncan, B. N., Froidevaux, L., Bhartia, P. K., Levelt, P. F., and Waters, J. W.: Tropospheric ozone determined from aura OMI and MLS: Evaluation of measurements and comparison with the Global Modeling Initiative's Chemical Transport Model, Journal of Geophysical Reseach - Atmospheres, 111, 10.1029/2006JD007089, 2006.

Ziemke, J. R., Oman, L. D., Strode, S. A., Douglass, A. R., Olsen, M. A., McPeters, R. D., Bhartia, P. K., Froidevaux, L., Labow, G. J., Witte, J. C., Thompson, A. M., Haffner, D. P., Kramarova, N. A., Frith, S. M., Huang, L. K., Jaross, G. R., Seftor, C. J., Deland, M. T., and Taylor, S. L.: Trends in global tropospheric ozone inferred from a composite record of TOMS/OMI/MLS/OMPS satellite measurements and the MERRA-2 GMI simulation, Atmos. Chem. Phys., 19, 3257-3269, 10.5194/acp-19-3257-2019, 2019.